



Utrecht University

Faculty of Science

PARTICLE TRAJECTORIES IN TOPOGRAPHY-INDUCED CURRENTS:
LOOKING FOR CHAOTIC BEHAVIOUR

Bachelor Thesis

Physics and Astronomy
Mathematics



Author
S.T. VAN DER WAL

Supervisors
H.E. de SWART
Department of Physics, UU
J.E. FRANK
Mathematical Institute, UU
G.P. SCHRAMKOWSKI
Flanders Hydraulics Research

Wednesday 20th January, 2021

Abstract

Tidal waves are experienced all over the world. In shallow tidal areas, the tidal current over a bottom-topography leads to induced residual currents. To study the effect of these residual currents in combination with the tidal current on the trajectories of passive particles, previous studies used a simplified Hamiltonian model. To compensate for the neglected terms, the relative strength of the residual currents was overestimated. It was shown that under certain circumstances the dynamics leads to chaotic particle trajectories in phase space. In this study it is shown that, up to first order, the chaotic behaviour, as previously found, is not as commonly present in these systems. Furthermore, this study tries to investigate the effect of adding the Coriolis-term, a vorticity-harmonic term and a divergent term, which were previously neglected, to the dynamics. The effects of adding these terms in the dynamical equations did not trigger the onset of chaotic particle trajectories. In order to compute these particle trajectories, a splitting method is adapted to fit the time-periodic forcing that is present in these tidal systems. In contrast to previously used methods, this numerical method preserves the symplectic structure of the time-evolution of a Hamiltonian system. In the order of hundreds of tidal periods, this method produces similar results to Runge-Kutta methods for the majority of the cases. For longer periods of time, the Runge-Kutta methods showed divergence of the particle trajectories, even when this is not expected by the dynamics equations. A special case in phase space was found for choosing typical parameters that link to the Bessel functions (Beerens, Ridderinkhof, and Zimmerman 1994). In these special cases the shape of the particle trajectories changes significantly. For future studies, this behaviour may be of interest. Future studies may also look at adding even more tidal constituents to the dynamics or investigating the effect of choosing a bottom-topography with different spatial form. The numerical method presented here, may be applied in different problems, where the system of interest (largely) obeys a symplectic nature and allows for a splitting method.

Contents

1	Introduction	1
2	Model Description	3
2.1	Equations for tidal and residual currents	3
2.2	Choosing a bottom-topography	5
2.3	Coordinate transformation	6
3	Hamiltonian Systems	8
3.1	Hamilton's equations	8
3.1.1	Non-autonomous systems	9
3.2	Poincaré section	10
3.3	Symplectic Map	11
3.4	Chaos	11
4	Numerical method	13
4.1	Splitting method	13
4.1.1	Splitting	13
4.1.2	Time-Periodic Forcing	15
4.1.3	Gradient flow	15
4.2	Explicit Form of the Hamiltonians and gradient	15
5	Methodology	17
5.1	Parameters	17
5.2	Experiments	17
5.2.1	System configurations	17
5.2.2	Numerical Method	19
5.3	Analysis	19
5.3.1	Tidal Poincaré Section	19
5.3.2	Largest Lyapunov Exponent	20
5.3.3	Numerical method	21
6	Results	22
6.1	System configurations	22
6.1.1	Simple Configuration	22
6.1.2	Additional Terms	24
6.2	Numerical Method	26
7	Discussion	28
7.1	Experiments	28
7.1.1	System Configurations	28
7.1.2	Numerical Method	28
7.2	Relation with Bessel functions	29
7.3	Model shortcomings	29
7.4	Future Research	30
8	Conclusions	31
	References	32
A	Mathematics	33
A.1	Trigonometric Identities	33
A.2	Harmonic Truncation	33

B	Matlab Code	34
B.1	orbit.m	34
B.2	onestep.m	35
B.3	cosgrad.m	36
B.4	lyapunov.m	37
C	Identification with earlier study	39

1 Introduction

This study focuses on the behaviour of trajectories of particles in currents over a time-independent bottom-topography (Robinson 1983) in shallow tidal areas with an irregular bottom topography. In these shallow tidal areas, the currents are very complex because of interaction of the tidal current with the bottom-topography. These interactions lead to many harmonics of the tidal wave, among which are the so-called residual currents. These residual currents are organized in cells around sand-banks, the so-called residual eddies. Figure 1 shows the residual currents in the western Dutch Waddensea. The joint action of the tidal current and these residual eddies can lead to chaotic particle trajectories (Ridderinkhof and Zimmerman 1992). However, the models used so far are either obtained from very sophisticated numerical methods, or from highly simplified models. Moreover, in both cases particle trajectories were calculated by applying numerical methods that are not optimal for these systems. The overall objective of this study is gaining more insight in behaviour of particle trajectories in systems of tidal currents and residual eddies, and improving on the numerical solving method for these systems.

Every now and then, we hear news of some type of contaminant that pollutes the seas. This can be some container filled with plastics that fell of a cargo ship, or an oil leakage from an oilrig. Predicting the spread of these contaminants is not very easy or straightforward. The processes that lie at the basis of this spreading are very complicated, and are strongly influenced by the current patterns for shallow tidal areas. Also, initial conditions are very important for predictions. The findings in this study may contribute to better understanding of these current patterns.

The water-movement in shallow tidal areas has previously been reduced to a 2D problem by Pasmantier 1988. In the study, a connection was made with studies done by Aref 1983 and Ottino 1990, who showed that particle trajectories as a consequence of 2D incompressible currents are described by the Hamiltonian canonical equations. For time-dependent Hamiltonians, the particle trajectories showed a chaotic nature, which is called Lagrangian chaos or chaotic advection. Both (Ridderinkhof and Zimmerman 1992) and (Beerens, Ridderinkhof, and Zimmerman 1994) showed that a simplified 2D depth-averaged model may lead to chaotic patterns and trajectories. In the study they assumed a tidal current plus a residual current, neglecting amongst others the Coriolis term, and also assumed the depth-averaged currents to be divergence-free, which in reality they are not. This simplified model was integrated with a standard ODE-solver, which does not preserve the symplectic structure of so-called Hamiltonian systems.

The two objectives that we focus on in this study are to investigate what happens when we do take several of the previously neglected terms into account, and if it is possible to use a numerical method that preserves the symplectic structure of a Hamiltonian system. This study includes the Coriolis term, a vorticity-harmonic term, which is a result of the periodic interaction of the tide with the bottom-topography, and the divergence term one-by-one. We investigate their influence on the behaviour of particle trajectories through phase space by comparing Poincaré sections of systems both including and excluding these terms. This study also assesses the changes in characteristics of numerical solutions when using a splitting method instead of a numerical method that is not symplectic. We may then compare the results of this splitting method with time-periodic forcing to the method of standard ODE-solvers with local error analysis.

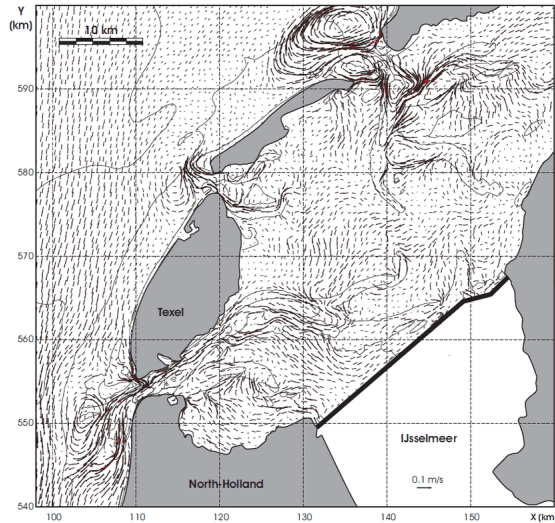


Figure 1: Residual currents in the western Dutch Waddensea (Giardino, Santinelli, and Heijer 2015).

The next three chapters go in on three aspects of the overall objective. The first chapter will talk at length about the model of the currents that is used and which assumptions are made. The second chapter gives the relevant theory of systems of differential equations and how to analyse them. The third chapter explains how the symplectic structure is maintained in the numerical method. Chapter 5 gives a description of the experiments and the parameter settings. One chapter later, the results are presented, divided into a section treating the results on particle trajectories with the extra terms, and a section showing the performance of the numerical method. Then follows a discussion and finally concluding remarks are given.

2 Model Description

2.1 Equations for tidal and residual currents

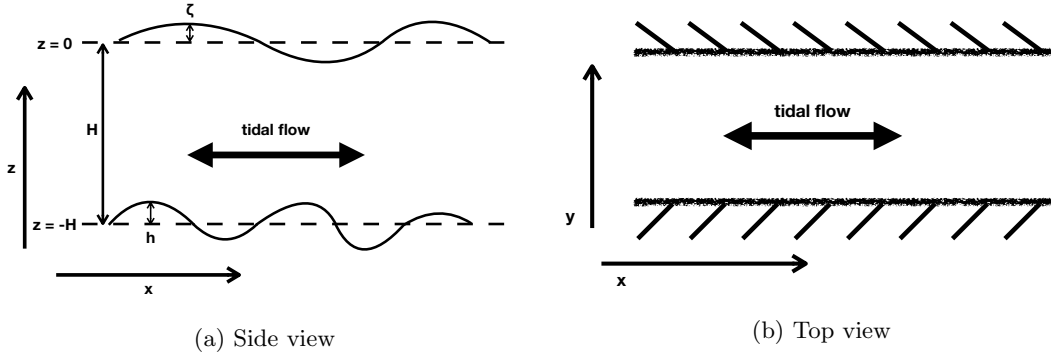


Figure 2: Graphical description of the modeled situation. Here, H is the average depth and the tidal flow is in the x -direction.

The currents in shallow tidal areas can be characterized by starting from the so-called shallow water equations, these follow from the Navier-Stokes equations by taking the limit

$$\frac{\text{vertical length scale}}{\text{horizontal length scale}} \rightarrow 0.$$

From the shallow water equations, the rigid-lid approach is taken, i.e. neglecting differences in water levels, but not the derivatives thereof. Assuming water with constant density it follows

$$\frac{\partial u}{\partial t} + u \frac{\partial u}{\partial x} + v \frac{\partial u}{\partial y} - fv = -g \frac{\partial \zeta}{\partial x} - \frac{ru}{H+h}, \quad (1a)$$

$$\frac{\partial v}{\partial t} + u \frac{\partial v}{\partial x} + v \frac{\partial v}{\partial y} + fu = -g \frac{\partial \zeta}{\partial y} - \frac{rv}{H+h}, \quad (1b)$$

$$\frac{\partial}{\partial x} [u(H+h)] + \frac{\partial}{\partial y} [v(H+h)] = 0. \quad (1c)$$

The first two are momentum equations and the last is the continuity equation which describes mass conservation. The parameters are

- u, v depth-averaged velocities in x, y direction,
- f Coriolis parameter (assumed constant),
- r linear bottom friction coefficient (assumed constant),
- t time,
- g acceleration due to gravity (assumed constant),
- h bottom height relative to the averaged depth,
- H average depth,
- ζ water-level difference ("ripple height").

It is convenient to replace the first two equations in (1) with the definition of vorticity η (equation (2a)) and an equation for the vorticity resulting from taking the x -derivative of (1b) and subtracting the y -derivative of (1a). This yields

$$\eta = \frac{\partial v}{\partial x} - \frac{\partial u}{\partial y}, \quad (2a)$$

$$\frac{\partial \eta}{\partial t} + u \frac{\partial \eta}{\partial x} + v \frac{\partial \eta}{\partial y} + (f + \eta) \left[\frac{\partial u}{\partial x} + \frac{\partial v}{\partial y} \right] = -\frac{\partial}{\partial x} \left(\frac{rv}{H+h} \right) + \frac{\partial}{\partial y} \left(\frac{ru}{H+h} \right), \quad (2b)$$

$$\frac{\partial}{\partial x} [u(H+h)] + \frac{\partial}{\partial y} [v(H+h)] = 0. \quad (2c)$$

In this study, we assume a model situation as shown in figure 2. This description places the x -axis in the direction of the tidal current. We can therefore define our depth-averaged velocities to be

$$\begin{aligned} u &= U(t) + \tilde{u}(t, x, y) \\ v &= \tilde{v}(t, x, y), \end{aligned} \quad (3)$$

where $U(t)$ is the tidal current and is given. It is assumed that the tidal current only depends on the time t . The components \tilde{u} and \tilde{v} are the currents induced by the bottom-topography. We now make the necessary assumption that the bottom height-variations are much smaller than the average depth, i.e. $[h] \ll H$ and also that the amplitude of the residual flow is much less than the length-scale on which the tide works, i.e. $[\tilde{u}], [\tilde{v}] \ll [U]$. Here $[.]$ denotes the typical magnitude of the parameter between brackets. Substituting (3) in into (2) and keeping only terms linear in the unknowns we obtain

$$\eta = \frac{\partial \tilde{v}}{\partial x} - \frac{\partial \tilde{u}}{\partial y}, \quad (4a)$$

$$H \left(\frac{\partial \tilde{u}}{\partial x} + \frac{\partial \tilde{v}}{\partial y} \right) = -U \frac{\partial h}{\partial x}, \quad (4b)$$

$$\frac{\partial \eta}{\partial t} + U \frac{\partial \eta}{\partial x} + \frac{r}{H} \eta = \left(\frac{f}{H} \frac{\partial h}{\partial x} - \frac{r}{H^2} \frac{\partial h}{\partial y} \right) U. \quad (4c)$$

The next step is to make (4) dimensionless via the introduction of

$$\begin{aligned} U &= [U]U', & h &= [h]h', \\ (x, y) &= \frac{[U]}{\sigma}(x', y'), & t &= \frac{t'}{\sigma}, \\ (\tilde{u}, \tilde{v}) &= \frac{[h]}{H}[U](u', v'), & \eta &= \frac{[h]}{H}\sigma\eta', \\ f &= \sigma f, & r &= \sigma H r', \end{aligned} \quad (5)$$

where σ is the tidal frequency, defined in relation with the tidal period (T) such that $\sigma = \frac{2\pi}{T}$. By substitution of (5) into (4) and dropping the primes we obtain the following equations of motion

$$\begin{aligned} \eta &= \frac{\partial v}{\partial x} - \frac{\partial u}{\partial y}, \\ \frac{\partial u}{\partial x} + \frac{\partial v}{\partial y} &= -U \frac{\partial h}{\partial x}, \\ \frac{\partial \eta}{\partial t} + U \frac{\partial \eta}{\partial x} + r\eta &= \left(f \frac{\partial h}{\partial x} - r \frac{\partial h}{\partial y} \right) U. \end{aligned} \quad (6)$$

Now the form of the bottom-topography h is defined. By defining the bottom-topography spatially, we can study what this implies for the currents. For this model we assume that our bottom-topography is described by a Fourier-series

$$h = \sum_{k'} \sum_{l'} \hat{h}_{k', l'} e^{i(k'x + l'y)}, \quad (7)$$

with $\hat{h}_{k', l'}^* = \hat{h}_{-k', -l'}$, this ensures that the bottom-topography is real-valued. The parameters k' and l' can be written as $k' = mk$ and $l' = nl$, where m, n take the place in the summation and k, l are

dimensionless wavenumbers, defined by

$$\begin{aligned} k &= \frac{2\pi[U]}{\sigma L_x}, \\ l &= \frac{2\pi[U]}{\sigma L_y}, \end{aligned} \quad (8)$$

with L_x and L_y the typical length scales in the x and y directions, respectively. This bottom topography restricts the solutions for u , v and η to be of the same form, meaning

$$(u, v, \eta) = \sum_m \sum_n (u_{k',l'}, v_{k',l'}, \eta_{k',l'}) e^{i(k'x+l'y)}. \quad (9)$$

Filling this in into equations (6) and combining the first two, we obtain expressions for $u_{k',l'}$ and $v_{k',l'}$

$$\begin{aligned} u_{k',l'} &= \frac{il'}{k'^2 + l'^2} \hat{\eta}_{k',l'} - \frac{k'^2}{k'^2 + l'^2} U \hat{h}_{k',l'}, \\ v_{k',l'} &= \frac{-ik'}{k'^2 + l'^2} \hat{\eta}_{k',l'} - \frac{k'l'}{k'^2 + l'^2} U \hat{h}_{k',l'}. \end{aligned} \quad (10)$$

The third equation results from filling (7) and (9) in into (6). This yields a solution for $\hat{\eta}_{k',l'}$. For this, a technique called 'harmonic truncation' is used, which is done in appendix A.2. From now on we assume that the tidal current is given by

$$U(t) = \cos t. \quad (11)$$

For this tidal current the result of harmonic truncation at truncation order $N = 1$ for η is

$$\hat{\eta}_{k',l'} = \eta_0 + \eta_{1c} \cos t + \eta_{1s} \sin t, \quad (12)$$

where the coefficients η_i are dependent on the parameters k' , l' , f , r , and $\hat{h}_{k',l'}$.

2.2 Choosing a bottom-topography

We have now identified expressions for $u_{k',l'}$, $v_{k',l'}$, and $\eta_{k',l'}$ as a function of the tide and the bottom-topography. The tide has been defined in equation (11). We now define the bottom topography to be

$$\begin{aligned} h &= \sum_{k'} \sum_{l'} \hat{h}_{k',l'} e^{i(k'x+l'y)} \\ &= \sum_{m \in \{1, -1\}} \sum_{n \in \{1, -1\}} \hat{h}_{k,1} e^{i(mkx+nl y)} \\ &= \frac{1}{4} e^{i(kx+ly)} + \frac{1}{4} e^{i(kx-ly)} + \text{complex conjugate}, \end{aligned} \quad (13)$$

at some value for k and l which are both positive numbers assumed to be known. Notice that we do not take into account terms with $m = 0$ or $n = 0$. What we have done is that we chose $\hat{h}_{k',l'} = \frac{1}{4}$, $\forall k', l'$, and chose m, n to be all combinations of $1, -1$. By adding the complex conjugate, we make sure our solution is strictly real. Figure 3 shows an example of what the bottom-topography (13) might look like for parameters $k = l = \frac{5}{\pi}$.

This choice of bottom-topography, results in restrictions on the solutions for u , v , and η , which will also be a summation over four complex exponential functions. Filling in (13) and (12) into (10), and doing some algebra and trigonometry (Appendix A.1) we end up with

$$\begin{aligned} u &= \cos t + \frac{[h]}{H} \left[\frac{lk}{(k^2 + l^2)(k^2 + 2r^2 + 2)} [rl \sin kx \cos ly - fk \cos kx \sin ly] \right] \\ &+ \gamma_1 \frac{[h]}{H} \left[\frac{2l(r \cos t + \sin t)}{(k^2 + l^2)(k^2 + 2r^2 + 2)} [fk \sin kx \sin ly + rl \cos kx \cos ly] \right] \\ &- \gamma_2 \frac{[h]}{H} \left[\frac{k^2 \cos t}{2(k^2 + l^2)} \cos kx \cos ly \right], \end{aligned} \quad (14)$$

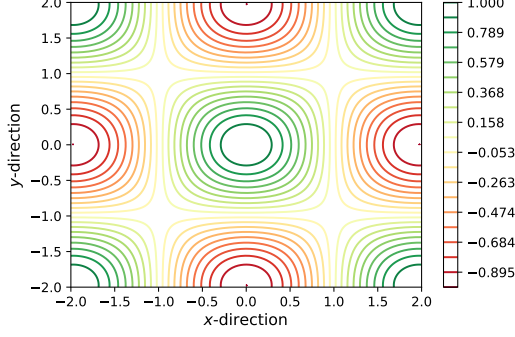


Figure 3: Example of the bottom-topography for $k = l = \frac{5}{\pi}$. The value at each point in the x, y -plane, is the bottom-height relative to the average bottom-height at that point in meters.

for u and for v we find

$$\begin{aligned}
 v = & \frac{[h]}{H} \left[\frac{k^2}{(k^2 + l^2)(k^2 + 2r^2 + 2)} [-rl \cos kx \sin ly + fk \sin kx \cos ly] \right] \\
 & + \gamma_1 \frac{[h]}{H} \left[\frac{2k(r \cos t + \sin t)}{(k^2 + l^2)(k^2 + 2r^2 + 2)} [fk \cos kx \cos ly + rl \sin kx \sin ly] \right] \\
 & - \gamma_2 \frac{[h]}{H} \left[\frac{kl \cos t}{2(k^2 + l^2)} \sin kx \sin ly \right],
 \end{aligned} \tag{15}$$

where a few new parameters entered the equations.

Let us start with $\frac{[h]}{H}$. This factor comes from the change in dimensions as done in (5). This factors in the relative height of the bottom-height variations $[h]$ to the average depth H . The bigger this factor, the bigger the relative strength of the topology-induced currents compared to the tidal current. Which is intuitively understood by the fact that steeper and higher bottom variations result in stronger induced currents. The other terms are γ_1 and γ_2 . These parameters are control-parameters. They control how extensive the model is. The value of these parameters is either 0 or 1. For a value of 0 the corresponding current is not taken into account, for a value of 1 it is. The γ_1 controls the vorticity harmonic term. This term is the result from the harmonic truncation result in (12). The term with γ_2 is the divergent term.

Now the explicit form of the model can be written down:

$$\begin{aligned}
 \frac{dx}{dt} &= u, \\
 \frac{dy}{dt} &= v,
 \end{aligned} \tag{16}$$

where u, v are defined by (14) and (15). In order to solve this numerically, it is useful to apply a coordinate transformation. The only purpose of the transformation is the easier numerical analysis.

2.3 Coordinate transformation

The transformation that will help us solve the system numerically is given by

$$\begin{aligned}
 q &= kx + ly, \\
 p &= kx - ly,
 \end{aligned} \tag{17}$$

with inverse transformation

$$\begin{aligned}
 x &= \frac{p + q}{2k}, \\
 y &= \frac{q - p}{2l}.
 \end{aligned} \tag{18}$$

The equations now take the form

$$\begin{aligned}
u = \cos t + \frac{[h]}{H} \frac{lk}{2(k^2 + l^2)(k^2 + 2r^2 + 2)} [(fk - rl) \sin q + (fk + rl) \sin p] \\
+ \gamma_1 \frac{[h]}{H} \frac{l(r \cos t + \sin t)}{(k^2 + l^2)(k^2 + 2r^2 + 2)} [(fk - rl) \cos q + (fk + rl) \cos p] \\
- \gamma_2 \frac{[h]}{H} \frac{k^2 \cos t}{4(k^2 + l^2)} [\cos q + \cos p],
\end{aligned} \tag{19}$$

for u and for v ,

$$\begin{aligned}
v = \frac{[h]}{H} \frac{k^2}{2(k^2 + l^2)(k^2 + 2r^2 + 2)} [(fk - rl) \sin q + (fk + rl) \sin p] \\
+ \gamma_1 \frac{[h]}{H} \frac{k(r \cos t + \sin t)}{(k^2 + l^2)(k^2 + 2r^2 + 2)} [(fk - rl) \cos q + (fk + rl) \cos p] \\
- \gamma_2 \frac{[h]}{H} \frac{k^2 \cos t}{4(k^2 + l^2)} [\cos q - \cos p],
\end{aligned} \tag{20}$$

where we used the trigonometric identities from Appendix A.1. After this coordinate transformation it is possible to write the equations as

$$\begin{aligned}
\frac{dp}{dt} &= -\frac{\partial H}{\partial q} - \frac{\partial V}{\partial p}, \\
\frac{dq}{dt} &= \frac{\partial H}{\partial p} - \frac{\partial V}{\partial q},
\end{aligned} \tag{21}$$

where H, V are functions of t, p and q . In this way of writing the equations of motion, the function $H(t, p, q)$ is called the Hamiltonian function and the function $V(t, p, q)$ the potential function. As will be explained in chapter 4, these functions can be even further split. These functions are widely studied and provide us with a lot of theoretical background. In chapter 3 the necessary theory on differential equations with Hamiltonian structure and how to characterize them is presented.

3 Hamiltonian Systems

In the next section the general properties of a Hamiltonian system will be briefly presented, including details on the symplectic structure of these systems. I will focus on systems that propagate in the x, y -plane. In section 3.4 the meaning of chaos and how this can be characterized is further explained.

3.1 Hamilton's equations

In equations (21) the dynamics were written as partly due to a Hamiltonian and partly due to a gradient flow. Here we will focus on the theory of Hamiltonian systems. Choosing $\gamma_2 = 0$, the function $V(t, q, p) = 0$, and the system in total becomes Hamiltonian, with equations of the form

$$\begin{aligned}\frac{dp}{dt} &= -\frac{\partial H}{\partial q}, \\ \frac{dq}{dt} &= \frac{\partial H}{\partial p},\end{aligned}\tag{22}$$

where p, q are the coordinates and $H(t, p, q)$ is the Hamiltonian function, or Hamiltonian. Many others have studied Hamiltonian systems, so describing the system this way can give us many insights in the dynamics.

For Hamiltonian systems where the Hamiltonian is time-independent we speak of an autonomous Hamiltonian system. For these systems the Hamiltonian is a conserved quantity, since along a solution

$$\frac{dH}{dt} = \frac{dp}{dt} \frac{\partial H}{\partial p} + \frac{dq}{dt} \frac{\partial H}{\partial q} = -\frac{\partial H}{\partial q} \frac{\partial H}{\partial p} + \frac{\partial H}{\partial p} \frac{\partial H}{\partial q} = 0.\tag{23}$$

Physically the Hamiltonian function in this case represents the total energy of the system. These systems have several theoretical benefits. From an initial condition, we can follow the time-evolution. This traces out a solution path. The solution path of particles in such a 2D autonomous Hamiltonian system describe unique solutions, that do not intersect one another in the p, q -plane. These solutions lie on so-called level sets of the Hamiltonian. It means that if you make a contour plot of the value of the Hamiltonian, it would show the same patterns as the solution paths of particles in the system. The mathematical space spanned by the coordinates p, q is called the phase space. All the solution paths of particles are defined in the phase space. A specific solution path that is followed by a particle with initial condition x_0 is called a trajectory or orbit through x_0 . For systems of autonomous differential equations, under relatively mild assumptions (Jordan and Smith 2007), we know that every position in the phase space lies on a unique orbit. Thus, following a particle with initial condition x_0 through phase space gives a unique path through phase space. These trajectories cannot cross each other, since that would break the uniqueness. It is possible to follow some particles with different initial conditions and to plot them in the same diagram. This would yield a diagram that shows some of the solution paths, such a diagram is called a 'phase portrait', because it portrays solutions through phase space.

Example 1. We can look at the residual flow of equations (14) and (15), i.e. setting $f = \gamma_1 = \gamma_2 = 0$, neglecting the tidal current $\cos t$, and also putting $k = l$ to simplify. This yields the dynamical system

$$\begin{aligned}\frac{dx}{dt} &= \alpha \sin kx \cos ky, \\ \frac{dy}{dt} &= -\alpha \cos kx \sin ky,\end{aligned}\tag{24}$$

with $\alpha = \frac{[h]}{H} \frac{rk}{2(k^2+2r^2+2)}$. This is an autonomous system that is described by Hamilton's equations with Hamiltonian $H(x, y) = \frac{\alpha}{k} \sin kx \sin ky$, so that

$$\begin{aligned}\frac{dx}{dt} &= -\frac{\partial H}{\partial y} = -\frac{\partial}{\partial y} \left[-\frac{\alpha}{k} \sin kx \sin ky \right] = \alpha \sin kx \cos ky, \\ \frac{dy}{dt} &= \frac{\partial H}{\partial x} = \frac{\partial}{\partial x} \left[-\frac{\alpha}{k} \sin kx \sin ky \right] = -\alpha \cos kx \sin ky.\end{aligned}\tag{25}$$

Figure 4 shows the phase portrait of this system. The trajectories do not cross, which is as it should.

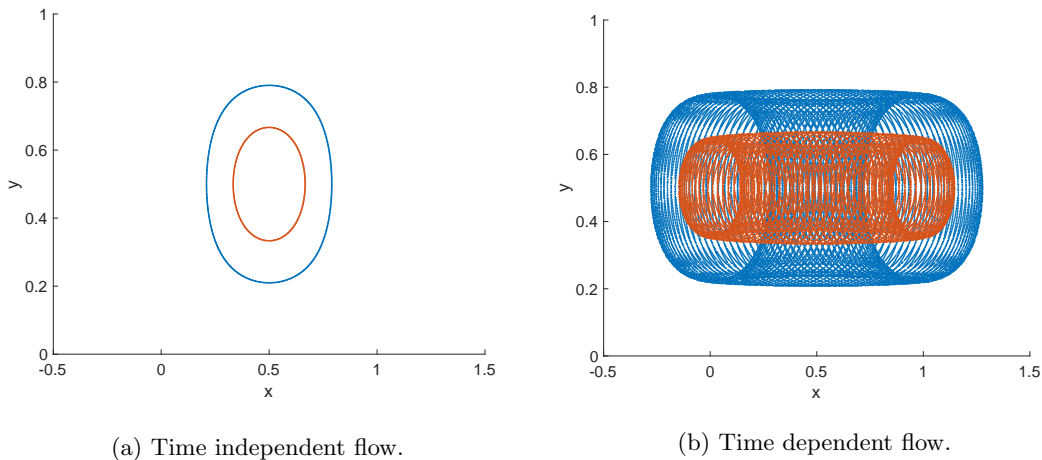


Figure 4: A phase portrait in the x, y -plane of an autonomous Hamiltonian system (left) and a non-autonomous Hamiltonian system (right). For the autonomous case, the particle trajectories lie on a closed line, that never cross another trajectory. In the non-autonomous case, the trajectories cross each other in the x, y -plane.

3.1.1 Non-autonomous systems

The problem that we are facing in the dynamical system that describes the model from chapter 2, is that the Hamiltonian function, in fact, is not time-independent. Our system is thus not an autonomous system and the Hamiltonian does not represent the conserved total energy. This also means that particle trajectories are not unique solutions in the p, q -space. Also, we cannot associate the particle trajectories with a level set of the Hamiltonian, since we simply can no longer make a contour plot of the Hamiltonian that is valid for every point in time. To tackle this, it is possible to add time as a dependent variable t to the differential equations by defining

$$\begin{aligned} t'(s) &= 1, \\ t(0) &= 0, \end{aligned} \tag{26}$$

where s takes the place as independent variable. Adding this to the system of equations, the t -dependence in the equations becomes a coupling with the now dependent variable t . We now, again, have an autonomous system on the phase space, but we have added another dimension to the 'phase space'. Furthermore, the system does not necessarily keep its Hamiltonian structure. It does, however, guarantee that particle trajectories through this three-dimensional 'phase space' do not intersect.

The next step is the visualization of these systems.

Example 2. Expanding the previous example with the addition of the tidal current $U = \cos t$, the system is no longer autonomous. The equations of motion now take the form

$$\begin{aligned} \frac{dx}{dt} &= \cos t + \alpha \sin kx \cos ky, \\ \frac{dy}{dt} &= -\alpha \cos kx \sin ky. \end{aligned} \tag{27}$$

This system can again be written as a Hamiltonian system, but not an autonomous one. Figure 4 shows the projection of the (x, y, t) movement onto the x, y plane. From this figure it looks as though these trajectories now intersect each other. Via the addition of the variable t as dependent variable, we could make this system autonomous again, regaining the condition that trajectories do not intersect

in phase space. The system now takes the form

$$\begin{aligned}\frac{dx}{ds} &= \cos(t(s)) + \alpha \sin kx \cos ky, \\ \frac{dy}{ds} &= -\alpha \cos kx \sin ky, \\ \frac{dt}{ds} &= 1.\end{aligned}\tag{28}$$

It is, however, not so easy to plot this. Especially for even higher dimensions, or many trajectories at once. Plotting many trajectories at once will produce some spaghetti-like diagram, from which it is very hard to deduce anything. The next section explains how this can be dealt with.

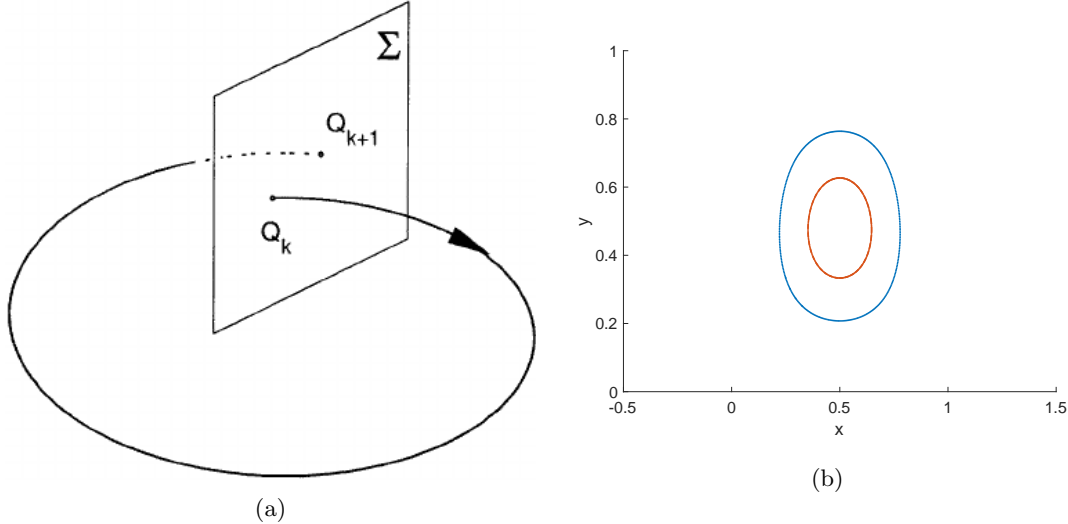


Figure 5: On the left a sketch of the general idea of the Poincaré section, obtained from Abdullaev 1999. Here the surface of section is denoted by Σ , and the point Q_{k+1} is the point where the trajectory first crosses the surface of section in the same direction after point Q_k . On the right, the tidal Poincaré section (TPS) of the example system described by equations (28).

3.2 Poincaré section

For the visualization of systems of differential equations that are not autonomous two-dimensional systems, there is a useful technique called a Poincaré section (Tabor 1989). The word section refers to the fact that we will take a section¹ of the phase space, by choosing a plane. Then we follow the time evolution of selected initial conditions along their trajectories through phase space, while marking the position where this trajectory crosses our surface of section. This way, a diagram is obtained with a collection of points that all lie in the same plane in phase space. Take for example a system with four-dimensional phase space with axes (q_0, q_1, p_0, p_1) , a Poincaré section could be constructed by choosing the plane $q_1 = p_1 = 0$ and starting from initial condition $q_0 = p_0 = 1$. Every time our solution crosses $p_1 = q_1 = 0$, the position on the q_0 - and p_0 -axis are marked. Figure 5 shows a simplified version of this. The resulting diagram shows a collection of points that all lie on the same trajectory. However, they may not appear in this diagram as a closed line, because they may be connected by a path that lies outside the plane $p_1 = q_1 = 0$.

So how can this technique be applied to the model of (21)? This system is two dimensional, but it is not autonomous. Thus, first the system has to be made autonomous by adding time t as a

¹"The cutting of a solid by or along a plane", Oxford University Press (2020). Available at: <https://www.lexico.com/definition/section> (Accessed: 6 January 2021).

third dimension, and we can then use the technique of a Poincaré section to visualize the resulting dynamics. For this we need to define the surface of section. To understand how a choice is made for the surface of section in this case, I recall here that the system is periodic in time. In other words, $H(t, p, q) = H(t + nT, p, q)$, with T the period of the tide and $n \in \mathbb{Z}$. We thus choose a surface of equal Hamiltonian as our surface of section.

The Hamiltonian reaches this equal value every tidal period. Thus all points in our Poincaré section differ an integer number of tidal periods from each other. The Poincaré sections of a system resulting from tidal currents will be called tidal Poincaré sections (TPS). Figure 5 shows the tidal Poincaré section for example 2 with time as dependent variable.

To summarize: Poincaré sections are useful for visualizing the time evolutions of systems of differential equations that have a phase space with a dimension higher than two. In this study, the tidal Poincaré section (TPS) shows the positions of particles at their initial condition and at their position an integer number of tidal periods later. If we look at 100 tidal periods, each particle would appear 100 times in the TPS. One for each tidal period. It can also be seen as a stroboscopic picture of particles, with a tidal period in between, which are then combined to create one diagram.

3.3 Symplectic Map

The consecutive points where a trajectory crosses the surface of section form a discrete map. This map is called a Poincaré map, because it maps points in the Poincaré section to the next point in the Poincaré section. For a tidal system, this mathematical mapping is called the discrete tidal map $x_{n+1} = \mathbf{T}(x_n)$. This mapping, can be approximated in several ways. In this study, the mapping is approximated numerically by the method described in chapter 4. A very important aspect of this numerical mapping is the notion of symplecticity.

Symplectic numerical methods are known to have advantageous properties for autonomous Hamiltonian systems. Backward error analysis (see Hairer et al. and Leimkuhler et al.) shows that the numerical solution of an autonomous Hamiltonian system by a symplectic numerical integrator approximates—to a much higher degree of accuracy than the formal order of the method—the exact solution of a modified system of equations, which is again a Hamiltonian system with a perturbed Hamiltonian function. Consequently, the numerical solution conserves the Hamiltonian up to bounded oscillations, and retains most invariant tori when applied to an integrable Hamiltonian system (KAM theorem). For nonautonomous systems, such as considered here, no such results are known. Our splitting method by construction, which essentially removes the nonautonomous forcing via a local time transformation of split subsystems, can be seen as an iterated symplectic map from Poincaré section to Poincaré section, and is therefore volume-preserving (e.g. introduces no numerical dissipation). However, since the Poincaré map is of finite length (equal to the period of tidal forcing), we cannot apply backward error analysis.

The composition of symplectic maps is again symplectic. This will be used in the numerical method. One particularly beneficial consequence is the fact that Hamiltonian systems are volume-preserving in phase-space. This means that if we take a three-dimensional cube in the phase space of system (28) and follow the time evolution, the volume of the cube is preserved. It may, however, be twisted and folded and stretched in all kinds of ways. A symplectic function or map, preserves this property as well, since it preserves the Hamiltonian structure. Thus, a symplectic map is volume-preserving in phase space.

3.4 Chaos

Intuitively, chaos can be understood as the unpredictability of solution paths in phase space. This occurs in many dynamical systems. Mathematically, a map is chaotic if it meets three conditions (Hirsch, Smale, and Devaney 2004). The two that are of interest here are

- Sensitive dependence on initial conditions;
- Each solution path eventually comes arbitrarily close to each point on some bounded set (sometimes called mixing).

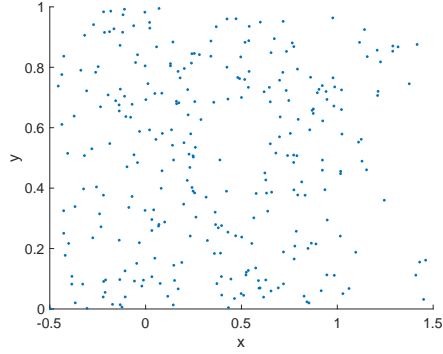


Figure 6: The collection of points where a chaotic trajectory crosses the surface of section. The initial condition was $(x, y) = (0.5; 0.7)$. This trajectory has numerical largest Lyapunov exponent $\lambda = 0.12$.

This means we have to define a way of knowing whether solutions are mixing, and also a measure of sensitivity to initial conditions. The mixing characteristic of a system can be checked visually via the TPS. A mixing region is a region where all solutions visit each point in this region. For regions where this is the case, the TPS should show some sort of confetti of points. The regular oval shaped orbits from figure 5 do not qualify for this. The trajectory in figure 6 shows what a chaotic trajectory might look like.

The other measure for chaos that is used in this study is the sensitivity on initial conditions. If the system is sensitive to initial conditions, two initially 'close' particles, will diverge exponentially. The rate of exponential divergence can be measured via Lyapunov exponents. To explain what Lyapunov exponents mean, the book Vulpiani, Cecconi, and Cencini 2009, section 5.3, is followed.

The stability of a trajectory can be quantified in relation to nearby trajectories. In non-chaotic regions or systems, the distance between neighbouring trajectories does not grow exponentially, which it does for chaotic systems. Here we follow the time evolution for a particle with initial condition \vec{x}_0 . We then study the distance with an initially close orbit $\vec{x}_0 + \delta\vec{x}(0)$, where $\Delta x(t) = \|\delta\vec{x}(t)\|$ is formally an infinitesimal length. If the system is chaotic the separation of these trajectories is described by

$$\Delta x(t) \sim \Delta x(0)e^{\gamma t}, \quad (29)$$

where γ is the local Lyapunov exponent and $\Delta x(t)$ is the distance to the perturbed trajectory from the reference trajectory at time t . The value of this Lyapunov exponent can, however, fluctuate along a trajectory. To overcome this, it is possible to define the maximum Lyapunov exponent by

$$\lambda_{\max} = \lim_{t \rightarrow \infty} \lim_{\Delta(0) \rightarrow 0} \frac{1}{t} \log \left(\frac{\Delta x(t)}{\Delta x(0)} \right). \quad (30)$$

When the value for λ_{\max} is positive it shows exponential divergence of trajectories and thus we say a trajectory is chaotic. In the case of no sensitivity of initial conditions, this limit yields a value of 0.

A Lyapunov exponent can be calculated for the dynamical system via equation (30). It is also possible to do this for a numerical method. This is shown in section 5.3.2.

4 Numerical method

The system of differential equations that describe a dynamical system may be very hard to solve analytically. It therefore seems very reasonable to construct a numerical method so that computers can calculate the trajectories of particles. Standard ordinary differential equations (ODE)-solvers use a variety of methods to approximate the trajectories numerically. A very common scheme is the Runge-Kutta scheme, which uses a combination of intermediate results to approximate the next position after an increase in time of Δt . One of the standard ODE-solvers that is built into Matlab, is ode45, which uses a fourth order Runge-Kutta method (Shampine and Reichelt 1997). These standard methods are, however, designed to fit a wide variety of systems of differential equations, and are therefore very general. This means that the method cannot be specified to a certain type of system, since it would not remain a general ODE-solver. A symplectic method is characterized by the fact that it preserves the Hamiltonian structure of the system that it tries to solve. A symplectic numerical method is thus a symplectic map. The standard methods are not symplectic in general. In this chapter a symplectic numerical method is presented.

4.1 Splitting method

A very useful technique for constructing a symplectic method is applying a splitting method. A splitting method is the splitting of the dynamics or mapping into several parts. If these individual parts are symplectic, the composition of these is again symplectic. The splitting method that will be used here results in a second order method. So, the downside is that we give away two orders of accuracy. The upside is that this method guarantees the preservation of the Hamiltonian structure of the system for all mappings that are due to a Hamiltonian described flow.

4.1.1 Splitting

Here a basic description of a splitting method (McLachlan and Quispel 2002) is given. The splitting in a splitting method is done in such a way that dynamics due to each part can be considered separately and integrated one after the other. After splitting the system in all the different parts, we have Hamiltonian and potential function

$$\begin{aligned}\tilde{H}(t, p, q) &= \tilde{H}_0(p, q) \cos t + \tilde{H}_1(p, q) + \tilde{H}_2(p, q)(r \cos t + \sin t) + \tilde{H}_3(p, q) \cos t, \\ \tilde{V}(t, p, q) &= \tilde{V}_3(p, q) \cos t.\end{aligned}\tag{31}$$

Here we see that the Hamiltonian and potential are split into products of functions of p and q with functions of time t . First, we treat the even further splitting of Hamiltonians $H_i(p, q)$. Then we deal with the time-periodic forcing. The splitting of the Hamiltonians $H_i(p, q)$ takes the form

$$H(p, q) = G(p) + F(q).\tag{32}$$

for which the Hamiltonian equations take the form

$$\begin{aligned}\frac{dq}{dt} &= \frac{\partial H}{\partial p} = G'(p), \\ \frac{dp}{dt} &= -\frac{\partial H}{\partial q} = -F'(q).\end{aligned}\tag{33}$$

To create a numerical method from these equations, the following scheme can be used for an increment of time Δt :

$$\begin{aligned}q_{n+1} &= q_n + \Delta t G'(p_n), \\ p_{n+1} &= p_n - \Delta t F'(q_n).\end{aligned}\tag{34}$$

The method hereabove is not symplectic in general. This can be seen by calculating the change in volume of the method. The change of volume can be calculated by

$$\frac{\partial(q_{n+1}, p_{n+1})}{\partial(q_n, p_n)} = \begin{vmatrix} 1 & \Delta t G''(p_n) \\ -\Delta t F''(q_n) & 1 \end{vmatrix} = 1 + \Delta t^2 G''(p_n) F''(q_n).\tag{35}$$

Since this determinant is not equal to one, the method is not volume-preserving and thus not symplectic. To construct a symplectic method, we treat the functions $F(q)$ and $G(p)$ as Hamiltonians on their own. Deriving for both these systems Hamilton's equations we have

$$\begin{aligned} q' &= G'(p), \\ p' &= 0, \end{aligned} \tag{36}$$

and

$$\begin{aligned} q' &= 0, \\ p' &= -F'(q). \end{aligned} \tag{37}$$

The first system has exact solution

$$\begin{aligned} q_n^* &= q_n + \Delta t G'(p_n), \\ p_n^* &= p_n. \end{aligned} \tag{38}$$

The second system has exact solution

$$\begin{aligned} q_{n+1} &= q_n^*, \\ p_{n+1} &= p_n^* - \Delta t F'(q_n^*). \end{aligned} \tag{39}$$

Composing these systems one after another gives the numerical method

$$\begin{aligned} q_{n+1} &= q_n + \Delta t G'(p_n), \\ p_{n+1} &= p_n - \Delta t F'(q_{n+1}), \end{aligned} \tag{40}$$

for which the method does preserve the area. This latter mapping is symplectic since both the individual systems are exact Hamiltonian flows, and thus symplectic. The order of p and q can be switched, making the adjoined method

$$\begin{aligned} p_{n+1} &= p_n - \Delta t F'(q_n), \\ q_{n+1} &= q_n + \Delta t G'(p_{n+1}), \end{aligned} \tag{41}$$

which is also a symplectic method, with the same level of accuracy. These methods are of first order accuracy. However, combining these methods, we can create a time-reversible symplectic second-order method. This method takes the form

$$\begin{aligned} q_{n+1/2} &= q_n + \frac{\Delta t}{2} G'(p_n), \\ p_{n+1/2} &= p_n - \frac{\Delta t}{2} F'(q_{n+1/2}), \\ p_{n+1} &= p_{n+1/2} - \frac{\Delta t}{2} F'(q_{n+1/2}), \\ q_{n+1} &= q_{n+1/2} + \frac{\Delta t}{2} G'(p_{n+1}), \end{aligned} \tag{42}$$

where the second and third row can be combined to one equation, to create the Störmer-Verlet method (Hairer, Lubich, and Wanner 2003):

$$\begin{aligned} q_{n+1/2} &= q_n + \frac{\Delta t}{2} G'(p_n), \\ p_{n+1} &= p_n - \Delta t F'(q_{n+1/2}), \\ q_{n+1} &= q_{n+1/2} + \frac{\Delta t}{2} G'(p_{n+1}). \end{aligned} \tag{43}$$

This concludes the treatment of the splitting of the Hamiltonian $H(p, q)$. The attention now turns to the time-periodic forcing.

4.1.2 Time-Periodic Forcing

The time-dependent dynamics are not autonomous. As we saw earlier, it is possible to add time as a dependent variable in order to make the system autonomous again. For the case of time-periodic forcing, this will be done via a time-transformation. To show how this works, we take an example Hamiltonian of the form $H(t, p, q) = \cos t(G(p) + F(q))$, yielding

$$\begin{aligned}\frac{dp}{dt} &= -\frac{\partial H(t, p, q)}{\partial q} = -\cos t F'(q), \\ \frac{dq}{dt} &= \frac{\partial H(t, p, q)}{\partial p} = \cos t G'(p).\end{aligned}\tag{44}$$

This system can be made autonomous using the transformation $\frac{d}{dt} = \frac{d}{d\tau} \frac{d\tau}{dt} = \cos t \frac{d}{d\tau}$. The corresponding Hamiltonian is $H(p, q) = G(p) + F(q)$. If we write the dynamics with this time-transformation and new Hamiltonian we obtain

$$\begin{aligned}\frac{dq}{d\tau} &= \frac{\partial H}{\partial p} = G'(p), \\ \frac{dp}{d\tau} &= -\frac{\partial H}{\partial q} = -F'(q).\end{aligned}\tag{45}$$

This leads to the numerical method

$$\begin{aligned}\Delta\tau &= \sin(t + \Delta t) - \sin(t) \\ q_{n+1} &= q_n + \Delta\tau G'(p_n), \\ p_{n+1} &= p_n - \Delta\tau F'(q_{n+1}).\end{aligned}\tag{46}$$

For different time-periodic forcing, different time-transformations are necessary. This time-periodic forcing is also present in the potential flow of the system.

4.1.3 Gradient flow

In equations (14) and (15) the last term, with the factor γ_2 , is the non-Hamiltonian term. This means that we cannot write these in the convenient way as we did with all the Hamiltonian parts. This also means that this term makes the dynamics no longer volume-preserving. The numerical mapping is therefore not symplectic (since there is no Hamiltonian structure to preserve). The dynamics due to these terms can be written as a gradient flow. As it turns out, this gradient flow can be further split into a part that is again Hamiltonian and a part that is a pure gradient flow. This paragraph explains how we deal with this latter 'pure' gradient flow. The potential function is of the form $V(p, q) = \gamma_2 \beta(\sin q + \sin p)$. Where γ_2 is again the control parameter and β is some function of $k, l, \frac{[h]}{H}$. This leads to the dynamics

$$\begin{aligned}\frac{dq}{dt} &= -\frac{\partial V}{\partial q} = -\gamma_2 \beta \cos q, \\ \frac{dp}{dt} &= -\frac{\partial V}{\partial p} = -\gamma_2 \beta \cos p.\end{aligned}\tag{47}$$

This splitted gradient results in two cases of the same form of dynamics. Therefore, we can solve these with the same function. The solution for this gradient flow is obtained via an iterative Newton's method. This is a discretized method with implicit midpoint, Newton's method is used to solve the implicit relations. The Matlab code for this can be found in appendix B.3.

4.2 Explicit Form of the Hamiltonians and gradient

The previous sections have described the techniques to transform the model from section 2 into a numerical model. In chapter 2 we saw in equation (21) that the dynamics in the p, q coordinates can

be written as a Hamiltonian and gradient. This Hamiltonian can be split in several parts, each with their own time-periodic forcing. These parts can again be split into one term independent on p and one term independent on q . This section presents the actual Hamiltonians and gradient used to calculate the particle trajectories. The full Hamiltonian and potential take the form

$$\tilde{H} = \tilde{H}_0 \cos t + \tilde{H}_1 + \tilde{H}_2(r \cos t + \sin t) + \tilde{H}_3 \cos t, \quad \tilde{V} = \tilde{V}_3 \cos t, \quad (48)$$

where \tilde{H}_0 corresponds to the tidal current, \tilde{H}_1 corresponds to the residual flow, \tilde{H}_2 corresponds to the γ_1 -term, and \tilde{H}_3 and \tilde{V}_3 correspond to the γ_2 -term. These have the form

$$\tilde{H}_0 = k(p - q), \quad (49)$$

$$\tilde{H}_1 = \frac{[h]}{H} \frac{-k^2 l}{2(k^2 + l^2)(k^2 + 2r^2 + 2)} ((fk - rl) \cos q + (fk + rl) \cos p), \quad (50)$$

$$\tilde{H}_2 = \gamma_1 \frac{[h]}{H} \frac{2kl}{2(k^2 + l^2)(k^2 + 2r^2 + 2)} ((fk - rl) \sin q + (fk + rl) \sin p), \quad (51)$$

$$\tilde{H}_3 = \gamma_2 \frac{[h]}{H} \frac{-k(k^2 - l^2)}{4(k^2 + l^2)} (\sin q - \sin p), \quad (52)$$

$$\tilde{V}_3 = \gamma_2 \frac{[h]}{H} \frac{k}{4} (\sin q + \sin p). \quad (53)$$

The Hamiltonians can all be split the way described in section 4.1. The next step is to put this into the computer. In this study, the trajectories are calculated using Matlab. The primary documents of code are given in appendix B.

5 Methodology

5.1 Parameters

These parameters refer to equations (14) and (15). The parameters that are not of interest are set to a default value. These are $\frac{[h]}{H}$ and the bottom friction coefficient r .

For r we choose the value $r = 2$. This model parameter is related to the real bottom-friction coefficient r^* via

$$r = \frac{r^*}{\sigma H}, \quad (54)$$

where $\sigma = \frac{2\pi}{T}$ is the tidal frequency at tidal period T and H is the average depth of the water. For a the values $[\sigma] = \frac{2\pi}{43200} \approx 1.4 \times 10^{-4}$ and $[H] = 10$, $r = 2$ corresponds to a value of $r^* \approx 2.8 * 10^{-3}$, which is a typical value for bottom-friction coefficients (Wang, Liu, and Lv 2014).

For the term $\frac{[h]}{H}$, which enters the equations when making them dimensionless, we put $\frac{[h]}{H} = 0.3$. This term is the relative height of bottom variations to average depth. We already assumed that $[h] \ll H$ and thus this fraction should not be big. There are several arguments for different depth-scales from which the biggest value for $\frac{[h]}{H}$ was chosen, i.e. $\frac{[h]}{H} = 0.3$. This biggest value is chosen, because we strongly suspect that bigger values for this parameter result in more chaotic behaviour. In other words, if there is chaotic behaviour in the system, it will be found more easily with a higher value of $\frac{[h]}{H}$.

Next, we take a look at our bottom-topography, and more specific at the values of k and l . These are defined by relation (8). In all our experiments we take $k = l$, in order to simplify the equations and thus assume a bottom topography that consists of cells that are rectangular in shape. This is essentially setting the typical length scale in the x -direction equal to the length scale in the y -direction, i.e. $L_x = L_y$. We can determine the k -value for which the relative magnitude of the residual current has its maximum, via explicitly calculating the derivative of the prefactor in equation (14). This was found to be around $k = \sqrt{2(r^2 + 1)}$, so that $r = 2$ yields $k_{\max} = \sqrt{10}$. This corresponds to a value of L_x that is similar in magnitude to $[U]$, which is several kilometers.

The numerical method is based on the theory of chapter 4. For this method, the choice of Δt is important. If a smaller time step is chosen, this leads to more accurate numerical approximations of the Tidal map. However, if Δt is too small, the computation time is really high. In this study the value is set to $\Delta t = \frac{2\pi}{N}$, with $N = 200$. In other words, a tidal period is split into 200 steps. This number was based on experience.

5.2 Experiments

In order to determine the effects of additional terms in the equations of motion, and if it is possible to use a symplectic method that preserves the symplectic structure of a Hamiltonian system, first 7 experiments regarding different configurations are done, all solved with the same numerical method. Next, the symplectic splitting method is compared to results of the standard ode45-solver of Matlab by solving the same systems.

5.2.1 System configurations

For each of the configurations, a set of 35 initial conditions is chosen. These are evenly divided in the 1 by 1 square between $x = 0$ and $x = 1$, and $y = 0$ and $y = 1$. Each row of initial conditions has its own colour. Figure 7 shows the positions of the initial conditions and their respective colour. For each initial condition, the time-evolution is computed using the techniques from section 4. The primary Matlab codes are included in Appendix B. Each configuration is evaluated for six different values of k : $\{1.0, 1.4, 1.5, 2.0, 2.7, 3.0\} * \frac{\pi}{2}$. These are the same values as used in Beerens, Ridderinkhof, and Zimmerman 1994. For each of these values the time evolution is numerically determined using the symplectic splitting method that was described in section 4.

In table 1 the different system configurations can be seen. The simplest configuration of the model follows from putting $\gamma_1 = \gamma_2 = f = 0$. This neglects the Coriolis term, the vorticity-harmonic term

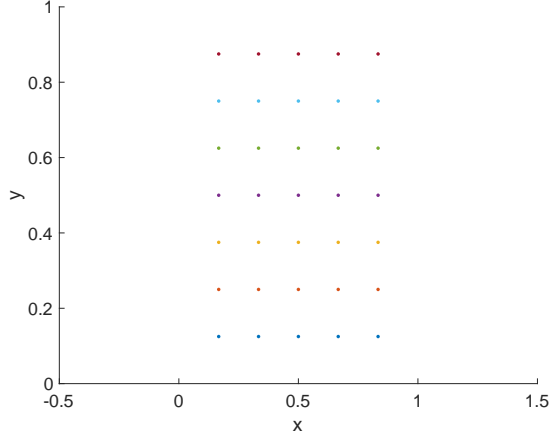


Figure 7: The initial conditions for the TPSs. Each row of points has a different colour.

and the divergent term in the dynamics completely. This configuration will be solved with two sets of parameters. One set resembles the system from an earlier study by Beerens, Ridderinkhof, and Zimmerman 1994. The other set resembles a similar configuration, but with a more realistic value for the relative strength of residual currents. These two parameter sets will be treated as different configurations. The set that resembles the earlier studies is called 'simple-b', whereas the set that resembles the realistic values is called 'default'. The former of the two uses a fixed value for the relative strength of the residual currents. The value that was chosen, however, cannot be matched by our default parameters. In order to create the same configuration as this previous study, the value for $\frac{[h]}{H}$ was turned into a function of k and r , i.e. $\frac{[h]}{H} = 0.6 \frac{k^2 + 2r^2 + 2}{kr}$. In Appendix C a more careful treatment of the transformation between both systems is given.

Besides the two simple configurations, there are four more. The first of these is the Coriolis configuration. This includes the Coriolis term by putting the Coriolis-parameter to $f = 1$. The rest of the parameters are set to default.

The next is the vorticity-harmonic configuration, where Coriolis-parameter is again $f = 0$, but now $\gamma_1 = 1$. This term resembles a time-dependent vorticity term, resulting from the harmonic truncation. These two configurations are combined in the sixth experiment called 'Cor-VortHarm'. The Coriolis parameter also effects the term with γ_1 , because this parameter influences the vorticity, and thus also the time-dependent term of the vorticity. Lastly the 'divergent' configuration is used by putting $\gamma_2 = 1$ and the rest to default. This term is evaluated via the potential function V from section 4.1.3. The different model configurations are shown in table 1. Each configuration is evaluated at six different values of k . These values are the same values as used by Beerens, Ridderinkhof, and Zimmerman 1994.

Experiment	Parameters				
	r	f	γ_1	γ_2	$\frac{[h]}{H}$
Default	2	0	0	0	0.3
Simple-b	2	0	0	0	$0.6 * \frac{k^2 + 2r^2 + 2}{rk}$
Coriolis	2	1	0	0	0.3
Vorticity-harmonic	2	0	1	0	0.3
Cor-VortHarm	2	1	1	0	0.3
Divergent	2	0	0	1	0.3

Table 1: Model configurations for each experiment. These parameters are filled in into equations (14) and (15) to obtain the governing equations.

5.2.2 Numerical Method

To test the quality of the numerical method that was shown in chapter 4, it will be compared to the standard ODE-solver of MATLAB, ode45. This latter solver is based on an explicit Runge-Kutta method (Shampine and Reichelt 1997). This method computes different solutions at intermediate points within the given time interval and uses these in a combination to produce the approximated solution for the end of the time interval.

To compare the methods, two identical codes are produced, where the only difference is the part where the numerical mapping of an initial position \vec{x}_n to the new position \vec{x}_{n+1} is done. Then, for both codes the same parameters are chosen and for 25 different settings the TPS is computed. The time it takes to produce these maps gives an indication of how fast each method is. This time can be obtained by using the 'run and time' button in Matlab. By also qualitatively comparing the resulting TPSs, both with each other and with the expectations, we obtain a more complete judgment of the numerical method.

5.3 Analysis

5.3.1 Tidal Poincaré Section

Each system configuration, with 35 initial conditions, leads to 35 lists of points. These points include all computed positions at every time step. From these points, only those that lie in the surface of section are of interest for our TPS. This means that for a time step $\Delta t = \frac{2\pi}{N}$ every N th position is of interest. Each of these points of interest are plotted in the x, y -plane. Thus the number of tidal periods is equal to the number of points in the TPS.

In section 3.4, I explained that chaos can be identified by mixing. If a system is mixing, this can be seen in the TPS. In the case of mixing, all points in the TPS belonging to the chaotic initial condition look like confetti. It is not necessarily the case that this includes the whole area between $x = 0$ and $x = 1$, and $y = 0$ and $y = 1$, but it may be some subset. By identifying the configurations and parameters for which this occurs, we can determine if the particle trajectories exhibit chaotic behaviour on some subset.

It could also be the case that the TPS shows no signs of mixing. In that case the consecutive positions of a particle trace out some sort of curve on the surface of section. These types of structures are called quasi-periodic, because they seem to repeat themselves over time. These quasi-periodic orbits look like closed lines in the TPS. These closed lines have some sort of midpoint. In the middle of these quasi-periodic orbits is, in fact, a periodic point, for which each consecutive point is mapped onto the previous one. These periodic midpoints, around which quasi-periodic orbits revolve, are called elliptic points. There is also another type of periodic point. This is the hyperbolic point, for which quasi-periodic orbits do not revolve around it, but rather move towards in one direction and move away in another direction. Figure 8 shows an example of both of these periodic points.

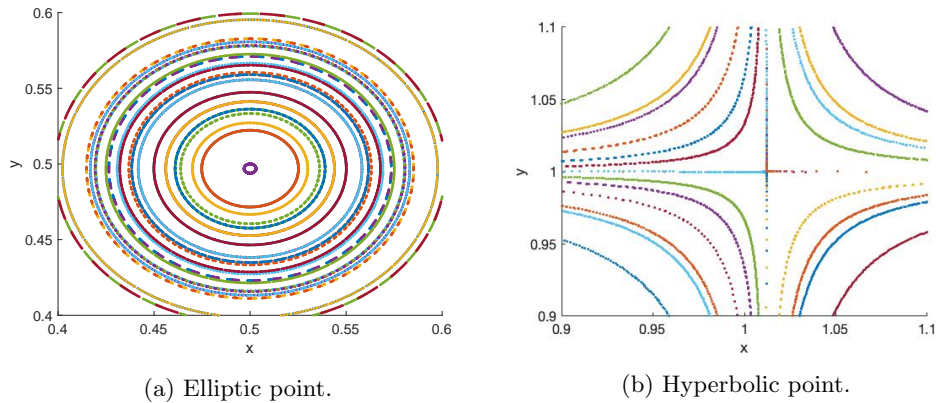


Figure 8: Two periodic points that might occur in the TPS with their respective neighbourhoods.

5.3.2 Largest Lyapunov Exponent

The other method to quantify chaos is the largest Lyapunov exponent. We will calculate here the largest Lyapunov exponent of the method, here shortened to λ . It is important to note here that the largest Lyapunov exponent of the method is not the same as the Lyapunov exponent of the underlying system of differential equations. Other numerical methods may find other values for λ . In this case, we are looking at the mapping

$$\vec{x}_{n+1} = \vec{F}_n(\vec{x}_n), \quad (55)$$

where $\vec{F}_n(\vec{x})$ is the numerical mapping that maps points in phase space to points at a time Δt later in phase space. The subscript on the function F_n indicates that the mapping depends on the time step. This method calculates the λ along all consecutive points that are numerical solutions to the differential equations that underlie this mapping for one initial condition. This means that we start from an initial condition and we calculate the rate of exponential separation at each time step Δt . The mean rate of exponential separation along a trajectory determines the value of λ . This depends on the rates of exponential separation in every point along the trajectory. To calculate the rate of exponential separation at a point, we choose an initial condition and a perturbation vector, which defines a perturbed initial condition. Now we numerically integrate both the initial condition and the perturbed point, and compute the distance of these after one time step. By comparing the perturbation after one time step to the initial perturbation, we get a measure of separation.

Consider initial condition $\vec{x}_0 = (x_0, y_0)$ and perturbation direction $\vec{v}_0 = (\delta x, \delta y)$, with $\|\vec{v}_0\| = 1$. The perturbation vector is the perturbation direction times a small distance $r_0 = \epsilon$. So that the perturbation is $\epsilon\vec{v}_0$. The perturbation after one time-step is

$$\vec{v}'_1 = \vec{F}'_0(\vec{x}_0) * \vec{v}_0 \approx \frac{\vec{F}_0(\vec{x}_0 + \epsilon\vec{v}_0) - \vec{F}_0(\vec{x}_0)}{\epsilon}, \quad (56)$$

where we used a linear approximation in the last step, and ϵ determines the quality of the latter approximation. In this study, this ϵ is, for reported values, set to 10^{-8} . Now define

$$\tilde{r}_1 = \|\vec{v}'_1\|, \quad (57)$$

which is the rate of separation from (x_0, y_0) to (x_1, y_1) . We now obtain the new perturbation direction via $\vec{v}_1 = \frac{\vec{v}'_1}{\tilde{r}_1}$. By repeating this process for the next iterations, the rate of separation at each point along a trajectory is calculated. These go into the formula for the mean rate of exponential separation. The mean rate of exponential separation is defined as

$$\begin{aligned} \Lambda &= \lim_{n \rightarrow \infty} \frac{1}{n} \log \frac{\tilde{r}_n}{r_0}, \\ &= \lim_{n \rightarrow \infty} \frac{1}{n} \log \left(\frac{\tilde{r}_n}{r_{n-1}} \frac{\tilde{r}_{n-1}}{r_{n-2}} \dots \right), \\ &= \lim_{n \rightarrow \infty} \frac{1}{n} \log \left(\frac{\tilde{r}_n}{r_{n-1}} \right) + \log \left(\frac{\tilde{r}_{n-1}}{r_{n-2}} \right) + \dots, \\ &= \lim_{n \rightarrow \infty} \frac{1}{n} \sum_{i=1}^n \log \frac{\tilde{r}_i}{r_{i-1}}. \end{aligned} \quad (58)$$

Remark: In our method $r_{i-1} = \|\vec{v}_{i-1}\| = 1 \quad \forall i$. This is because we rescale our vector after each iteration to have length 1. The formula for the estimated largest Lyapunov exponent, after N iteration steps, thus becomes

$$\lambda = \frac{1}{N} \sum_{i=1}^N \log \tilde{r}_i. \quad (59)$$

In this study, I use a time step of $\Delta t = \frac{2\pi}{200}$ and 50.000 tides to compute the largest Lyapunov exponent. This is equal to $N_{\text{steps}} = 10^7$ iterations. The initial perturbation direction is $\vec{v} = (1, -1)$. The Matlab code can be found in appendix B.4

To determine whether the value of λ converges to some positive value, or to 0, the evolution of the factor λ , with increasing N , is studied and compared to the behaviour of the function $1/x$. The latter shows a straight descending line when plotted in on a logarithm-logarithm scale. If the value for λ shows the same pattern with increasing N , the value of $\sum_{i=1}^N \log \tilde{r}_i$ remains constant with increasing N , which leads to a function that looks similar to $\frac{1}{x}$, hence we say λ converges to 0. If the value converges to some other value this can also be seen, namely the diagram of λ with increasing N shows a horizontal line. Two examples are given in 9, one of which converges to zero, the other converges to some positive value. We say that in the case of convergence to zero, the value of the LLE is $\lambda = 0$. In the other case the we have $\lambda > 0$, thus this configuration is at that point sensitive to initial conditions.

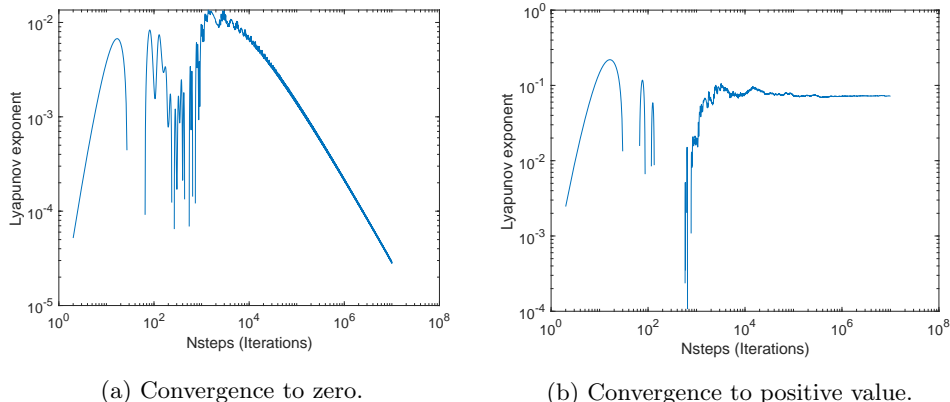


Figure 9: The evolution of the largest Lyapunov exponent for two different configurations and set of parameters. On the left a LLE that decreases with increasing iterations. In that case we say the LLE is zero. On the right the LLE converges to a positive value, this point is said to have a positive LLE and can be called chaotic in that sense.

5.3.3 Numerical method

From the numerical methods, we obtain two types of data. The first is the computation speed in seconds. The second is the qualitative results in the form of tidal Poincaré sections. The computation times can be analyzed by plotting them and seeing the relation between the two. It is expected that the symplectic splitting method needs less time to compute the time evolution for the same time step Δt than the ode45-solver. This is because the ode45-solver uses intermediate steps to calculate the displacement after a time Δt , where the symplectic splitting method only needs the previous position.

The second way in which both methods are compared, is the qualitative outlook of the TPS. This has two parts. From experience, it is known that some parameter settings showed different structures than the simplest one. For these cases we compare the qualitative results from both methods. Also on the long-term the symplectic splitting method is expected to preserve certain structures. Therefore, the long-term TPS of the simple configuration is compared. In this latter experiment there is only one initial condition. This is integrated over 2000 tidal periods.

6 Results

6.1 System configurations

6.1.1 Simple Configuration

The TPSs for the simple configuration are shown with two different parameter settings. The first that is shown is the parameter setting that reproduces the system used in Beerens, Ridderinkhof, and Zimmerman 1994. This is shown in figure 10. The results of the same configuration with the default parameter setting is shown in figure 11.

The TPSs of system 'simple-b' look very similar to the diagrams shown in the original study. For $\lambda_b = 1.0$, mainly quasi-periodic orbits are visible as avocado-shaped lines. Around the point $(x, y) = (0.5; 0.35)$ the central elliptic point can be located. Outwards from there, most of the collection of points produces a closed-looking line. Around the point $(x, y) = (0; 0.1)$, we find a so-called island. This is the result of an orbit that goes from one island to another in consecutive passings through the surface of section. The outermost points are the red dots that exhibit the confetti-like structure that is expected for mixing regions. The initial conditions that correspond to these orbits are $(x_0, y_0) = (\frac{1}{6}, \frac{7}{8})$ and $(x_0, y_0) = (\frac{5}{6}, \frac{7}{8})$. With respective largest Lyapunov exponents of $\lambda = 0.017$ and $\lambda = 0.020$.

In figure 10b we see that there are now 2 elliptic points, instead of one. This means that the central elliptic point has bifurcated into two, and in between lies a hyperbolic point. For this case there are no islands as in 10a and also no signs of a mixing region. For $\lambda_b = 1.5$, there has been even one more bifurcation. The diagram now shows 3 elliptic points aligned on the line $x = 0.5$. For this TPS, there is again no sign of mixing. The case $\lambda_b = 2.0$ clearly shows significant signs of mixing regions. Centered around $(x, y) = (0.5; 0.3)$, a three-lobbed figure can be found. A little bit further out, the trajectories show mixing behaviour. This behaviour is even more present in the cases where $\lambda_b = 2.7$ and $\lambda_b = 3.0$. In these latter two, there is little sign of non-mixing regions. They exist, however, but are rather small regions. For these regions that show signs of mixing, the largest Lyapunov exponent is for each individual initial condition larger than 10^{-2} .

Comparing the TPSs of the same configuration with default parameters, shows very different patterns and much less variation with topographic wavenumber k . All situations now show large regions of quasi-periodic orbits, with one central elliptic point. This central elliptic point is not in exactly the same place for each system. We do see, however, that for figure 11c the quasi-periodic orbits have holes in them. This is the result from the fact that the distance that a particle moves in a single tidal period is much less than the other cases.

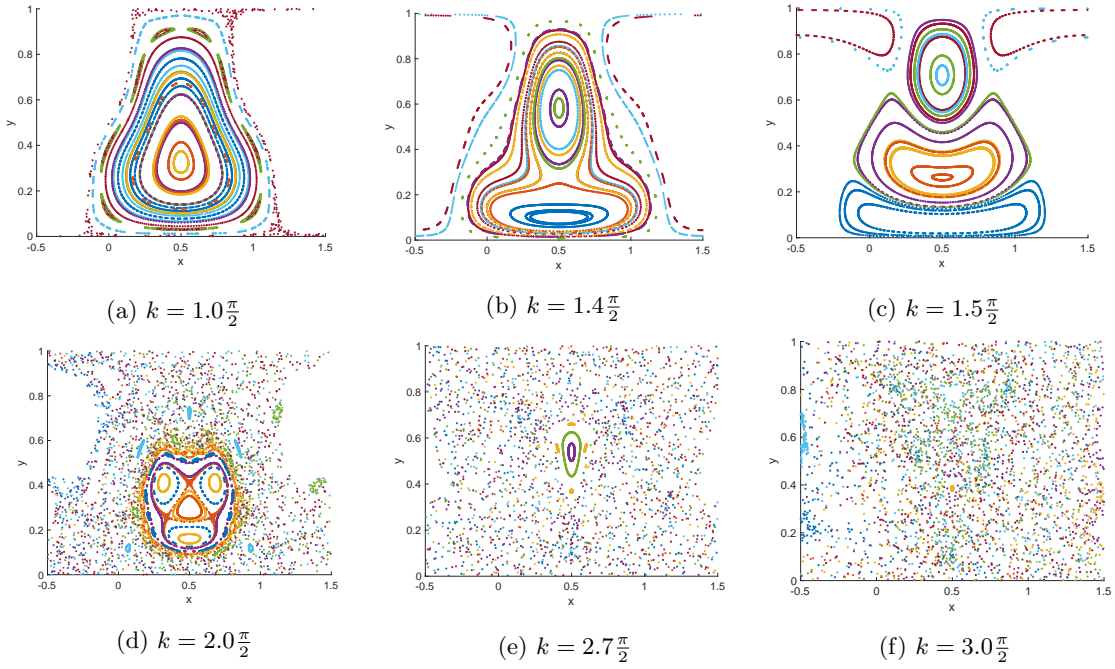


Figure 10: TPSs for the 'simple-b' configuration, for different values of k . These TPSs show that for $k > 1.5 \frac{\pi}{2}$ the system shows a confetti-like structure as expected for mixing regions. The Lyapunov exponent for these regions also converges to a positive value bigger than 10^{-2} .

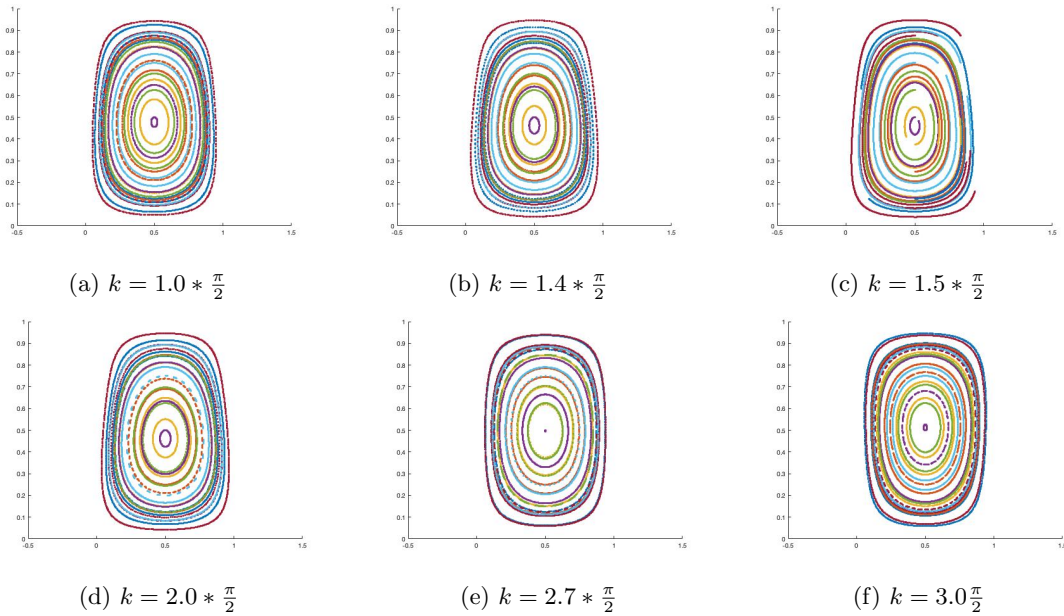


Figure 11: TPSs for the 'default' system, for different values of k . All TPSs show quasi-periodic orbits revolving around a central elliptic point. For $k = 1.5 * \frac{\pi}{2}$, the quasi-periodic orbits do not complete the full rotation.

6.1.2 Additional Terms

The other configurations were also numerically solved and for each the TPS was produced. Many of these look very similar to each other. Therefore, not all TPSs are shown. In figure 12 we see two columns of TPSs, The left column shows the four different configurations with additional terms for $k = 1.4 * \frac{\pi}{2}$, while the right column shows the same configurations with $k = 2.7 * \frac{\pi}{2}$. Only two of the six results is shown for each configuration, because the other TPSs showed very similar results.

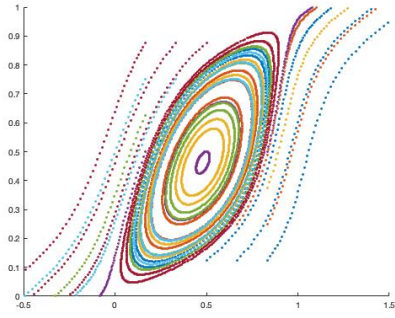
Figures 12a and 12b show the resulting TPSs for the Coriolis-configuration. In both cases, the shape of the quasi-periodic orbits has changed to a wedge-shape. This shape is tilted towards the line $x = y$. Initial conditions lying close to either the corner $(x, y) = (0, 1)$ or $(x, y) = (1, 0)$ do not show the same pattern as the quasi-periodic orbits. These particles leave the circulation cell. This in contrast to the particles in the default and simple-b configurations. In fact, zooming out, we see that these particles keep moving away from their initial conditions. The particles with initial conditions close to $(1, 0)$ go in the positive x and positive y direction, and the particles with initial conditions close to $(0, 1)$ move to the negative x and negative y directions. The central elliptic point is in both cases still present.

Figures 12c and 12d show the TPSs of the configuration 'Vorticity-Harmonic'. Both TPSs look very similar to the TPSs of the default configuration. The quasi-periodic orbits are still present. Also the central elliptic point is again present.

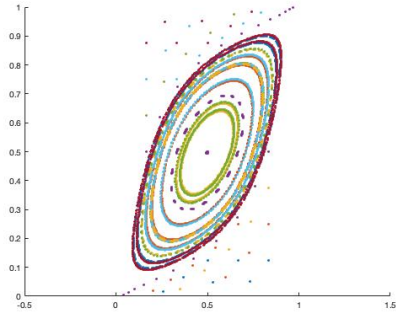
The configuration 'Divergent', with $\gamma_2 = 1$, is shown in figures 12e and 12f. These TPSs look a bit more blurry than the previous TPSs. This is because the position of a particle no longer lies on a quasi-periodic orbit, but slowly spirals outward. This results in a layer of points that are all due to one initial condition that occupy a 'band' in phase space. Even though, in 12f it looks like the central elliptic point is there, when zooming in, it can be shown that this is also an outward spiralling trajectory, moving away from the middle.

The last two TPSs, figure 12g and 12h, are the result of the configuration with $f = \gamma_1 = 1$, called 'Cor-VorHarm'. This TPS shows a very big resemblance to the TPSs from the Coriolis configuration in terms of shape. Again, we see the wedge-like shape in the TPS, with points on two sides of this wedge. These points, again, move away from this cell and do not return.

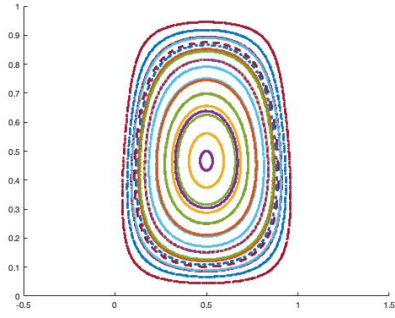
For the configurations 'default', 'simple-b', 'Coriolis', 'Vort-Harm' and 'Cor-VortHarm' the largest Lyapunov exponent was calculated for all the initial positions, with $k = 2.7 * \frac{\pi}{2}$. Only the 'simple-b' configuration had initial conditions with a largest Lyapunov exponent that was non-zero. For this configuration only three initial conditions had a to zero converging largest Lyapunov exponent. All other initial conditions showed a largest Lyapunov exponent with values $0.12 < \lambda < 0.13$.



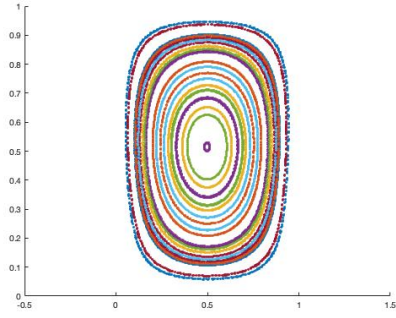
(a) Coriolis, $k = 1.4 * \frac{\pi}{2}$



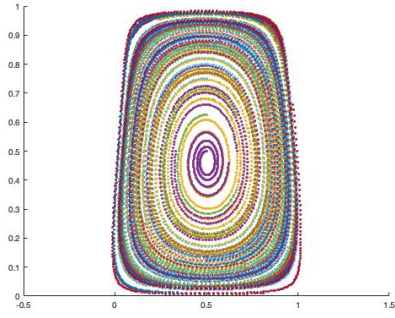
(b) Coriolis, $k = 2.7 * \frac{\pi}{2}$



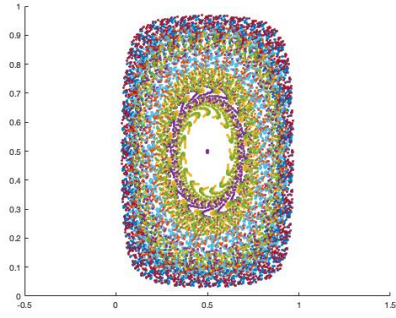
(c) Vort-Harm, $k = 1.4 * \frac{\pi}{2}$



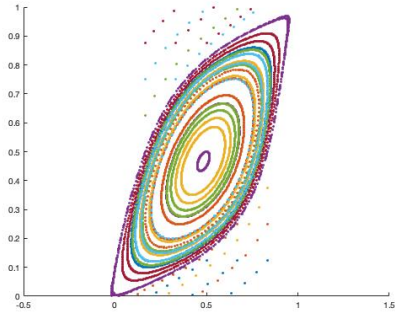
(d) Vort-Harm, $k = 2.7 * \frac{\pi}{2}$



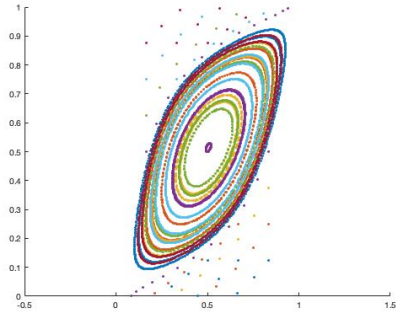
(e) Divergent, $k = 1.4 * \frac{\pi}{2}$



(f) Divergent, $k = 2.7 * \frac{\pi}{2}$



(g) Cor-VortHarm, $k = 1.4 * \frac{\pi}{2}$



(h) Cor-VortHarm, $k = 2.7 * \frac{\pi}{2}$

Figure 12: Representative TPS results for the model configurations 'Coriolis', 'Vort-Harm', 'Cor-VortHarm', and 'Divergent'. Each configuration is shown for both $k = 1.4 * \frac{\pi}{2}$ and $k = 2.7 * \frac{\pi}{2}$.

6.2 Numerical Method

First, I will discuss the computation time of the methods. To compare, both methods were given the same number of tidal periods and also the same number of intervals within a tidal period (N). The results in figure 13 show that the splitting method needed far less time to complete the computations. Differing from 6 to 70 times less computation time. This extra time comes from the fact that the ode45-solver uses a fourth order Runge-Kutta method (Shampine and Reichelt 1997) that approximates the next position. The symplectic splitting method does a simple computation using only the parameters and the previous points, whereas Runge-Kutta methods compute intermediate points in order to compute the position after a time Δt .

In figure 14, the long term time evolution is shown for the initial condition $(x, y) = (\frac{1}{3}, \frac{5}{8})$, computed with both the ode45-solver and the symplectic splitting method. The time intervals are not equal in this case. This is because in a normal setting the splitting method would have a defined fixed time step of $\Delta t = \frac{2\pi}{N}$, where $N = 200$, in our default case. For the ode45 method, a time interval is one of the parameter inputs of the function. The function itself, then, returns the fourth order approximation of the next position, after one tidal period. In this diagram, it is shown that for 2000 tidal periods, the symplectic splitting method produces a collection of points that lie on a closed line. This is a quasi-periodic orbit. For the ode45-solver case, the points do not all lie on the same line. This shows that after a longer time, 1000 tidal periods or more, the effects of not preserving the symplectic structures are visible.

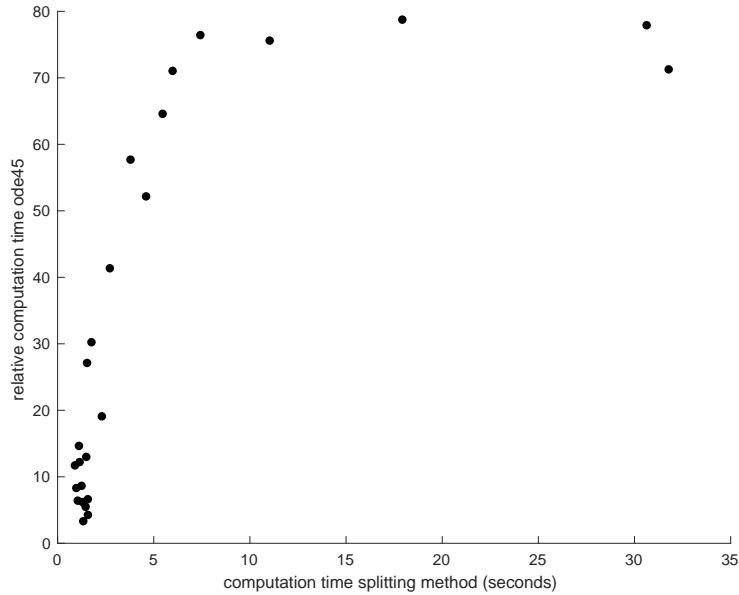
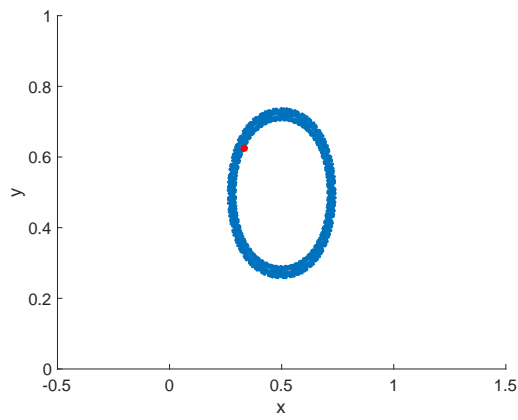
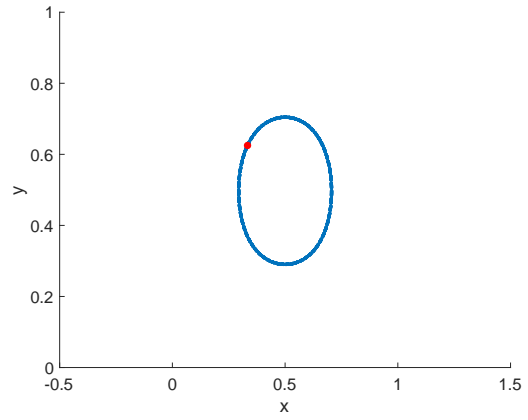


Figure 13: Computation time in seconds for the splitting method (x -axis) and the relative computation time of the Runge-Kutta method to the splitting method (y -axis).

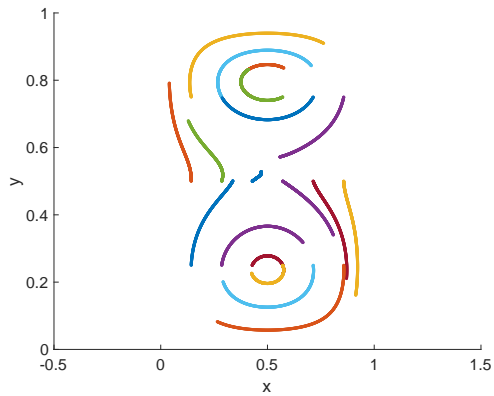


(a) Symplectic splitting method.

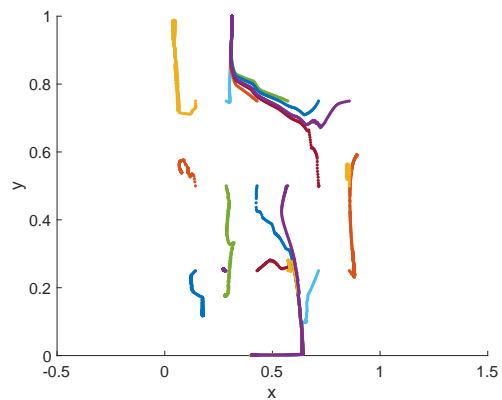


(b) Ode45-solver.

Figure 14: TPS for the 'Default' configuration with $k = 2.7 * \frac{\pi}{2}$, solved using two different numerical methods.



(a) Symplectic splitting method.



(b) Ode45-solver.

Figure 15: Two TPSs of the same system, obtained with different numerical methods. The system that was solved is the 'default' configuration with $k = 3.5 * \frac{\pi}{2}$.

7 Discussion

7.1 Experiments

7.1.1 System Configurations

The different system configurations revealed different structures. These were visible in the TPS. For the simplest configuration, the choice of $\frac{[h]}{H} = 0.6 \frac{k^2 + 2r^2 + 2}{kr}$ (simple-b) was used to recreate the system used in the study done by Beerens, Ridderinkhof, and Zimmerman 1994. The TPSs presented here, showed very similar patterns to this previous study. One of the differences that was found, is that for $k = 1.0 * \frac{\pi}{2}$ there were two chaotic trajectories. These trajectories were not found by Beerens, Ridderinkhof, and Zimmerman 1994. However, this choice for $\frac{[h]}{H}$ is not realistic, because this would have $[h] > H$, which by assumption is not the case. This is also logically not a realistic choice, since this would imply that the bottom-height variations ($[h]$) are bigger than the average depth H , thus the highest point in the bottom-topography would be above sea-level.

When a more realistic choice is made for $\frac{[h]}{H}$, the chaotic structures configuration simple-b were not reproduced. Moreover, the TPSs for this configuration (default) showed very similar results for values of k varying between $1.0 * \frac{\pi}{2}$ and $3.0 * \frac{\pi}{2}$. This showed that the strong k -dependence is not present for this set of parameters. One feature that was visible in the TPS for this configuration with $k = 1.5 * \frac{\pi}{2}$ was that the consecutive points in the TPS seemed to be very close to each other. This phenomenon is further discussed in section 7.2. The other four configurations also showed little k -dependence, except for the value $k = 1.5 * \frac{\pi}{2}$.

The Coriolis configuration showed a change in shape of the quasi-periodic orbits. The more interesting feature of these TPSs, however, is the fact that some particles, with initial conditions in the upper-left and down-right corner, moved away from there initial condition and did not describe a quasi-periodic orbit. This net transport of particles is a big difference to the other configurations and was only found in those systems where $f = 1$. Physically this means that water particles can travel great distances as a consequence of topography-induced currents.

The vorticity-harmonic configuration showed few big changes compared to the simple configuration. One interesting change, however, is the fact that the special k -dependence was not found for $k = 1.5 * \frac{\pi}{2}$ as it was for the simple configuration. The combination of these two configurations in the 'Cor-Vort-Harm' showed a mix of the two effects. The TPSs reflected the change of shape and transport of particles attributed to $f = 1$, while also losing the special k -dependence at $k = 1.5 * \frac{\pi}{2}$.

The configuration with the divergent term showed a spiralling outward of the consecutive particle positions. During some additional experiment, it was found that this spiralling outward also occurs for the same configuration with initial conditions lying one circulation cell further. This does, however, create a problem for the continuity of the current. Since these neighbouring circulation cells both show outward spiralling particles, this means that the particles would accumulate on the cell boundaries. This is physically not well-interpreted, since there seems to not be a tendency of water to accumulate on certain lines in the sea. Probably, this description needs taking into account of other effects such as diffusion, 3D-effects or water-level differences. These were all neglected in this study.

7.1.2 Numerical Method

The comparison of the computation time of both methods showed that for equal time step Δt , the symplectic splitting method, needed less time than the ode45-solver. In some cases this method needed 70 times less seconds. However, the ode45-solver could also be used by feeding it a time-interval such as a full tidal period, instead of small time steps Δt . This would allow the method to need less time in order to compute the position at one tidal period later. This does, however, decrease the quality of the resulting TPS. This was demonstrated by the two following experiments. Those experiments showed that the ode45-solver could not reproduce a sensible TPS when faced with the value $k = 3.5 * \frac{\pi}{2}$. By forcing the method to split this time interval into smaller time step Δt can help overcome this problem, but this means that it will be much slower.

Another example of where the results of both methods is not the same, is for a large number of tidal periods. The symplectic splitting method guarantees that the particle is in a quasi-periodic orbit. This is reflected by the fact that the consecutive plotted points form a closed-looking line. The ode45-solver, however, produced a TPS where the position of the particle slowly spirals outward. This phenomenon would not severely affect qualitative studies for a smaller time period, i.e. less than 1000 tidal periods. For longer periods of time, this might form a problem. Especially considering the fact that this type of structure in the TPS was found for the configuration with a divergent term. This may lead to the conclusion that the tidal map exhibits divergent features, even though this may not be due to the equations of motion but rather the numerical method.

7.2 Relation with Bessel functions

The special k -dependence at $k = 1.5 * \frac{\pi}{2}$ that seemed to 'slow down' the particles position in the TPS was found in many other cases, such as $k = 3.5 * \frac{\pi}{2}$ and $k = 5.5 * \frac{\pi}{2}$. For these latter cases, the TPS even showed a bifurcation of the central elliptic point into two elliptic points. This is shown in figure 16. We see two examples of a bifurcated central elliptic point. This was also found by Beerens, Ridderinkhof, and Zimmerman 1994 for $\lambda_b = 1.5$, which translates to $k = 1.5 * \frac{\pi}{2}$. Via a numerical technique called orbit expansion, they wrote down an explicit form of the tidal map. The second order analytic approximation to this map revealed a proportionality to the value of the Bessel function $J_0(k)$. The zeros of this function are very close to $k_n = (2n - \frac{1}{2}) \frac{\pi}{2}$, which are the values for which we saw the 'slowing down' of particles in the TPS, and also the bifurcated cases from figure 16. This does, however, imply that for the exact zero of this Bessel function, the TPS would look like the identity map. This was not confirmed by our methods. Also a decrease of the time step did not approximate the identity map any closer. An interesting study in this regard may be Benettin and Giorgilli 1994. Their study concerned symplectic mappings that are close to the identity map.

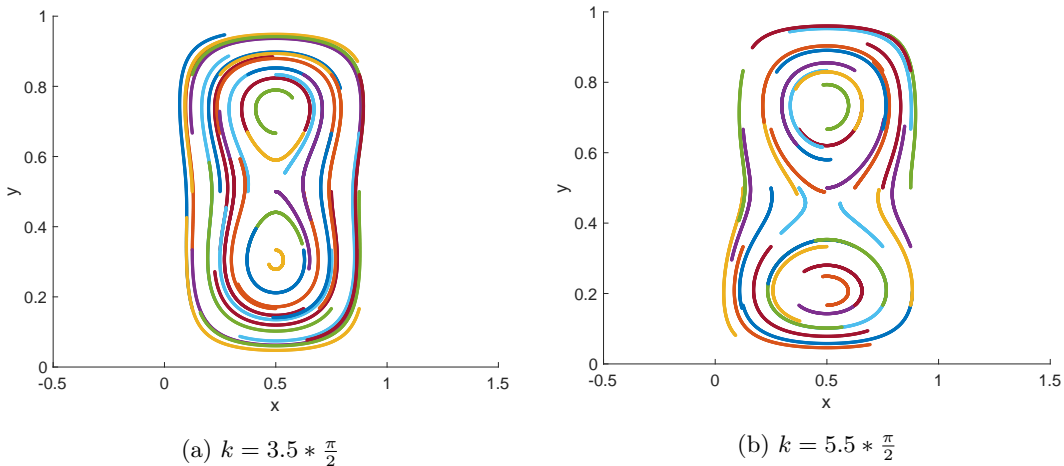


Figure 16: TPSs for the 'Default' configuration with two different cases that show a bifurcation of the central elliptic point into two elliptic points. In between a central hyperbolic point is formed.

7.3 Model shortcomings

One of the shortcomings in this study may be the highly simplified bottom-topography. The bottom-topography in this study is repeating, symmetric with respect to a ninety degrees rotation, and only consists of 4 Fourier modes, two of which are used to make sure the bottom-height variations are real-valued. These simplifications made analysis more easy but may have neglected some features. For instance, a choice of $k \neq l$ might be interesting to investigate. This seems also more realistic to me, since sandbanks may look like long ridges instead of round bulbs.

The currents themselves are also a highly simplified version of the actual currents in a tidal system. In this study, the currents consist of one tidal current plus at most four other components. Both the tidal current and the other terms can be improved upon. The tidal current, in reality, is made up of more than 100 components (Zervas 1999). Many of these have a small amplitude, but some of them are of reasonable strength to be taken into account. This does, however, create an extra challenge for the symplectic splitting method. By adding more tidal components, the Hamiltonian function describing these systems now has a different periodicity. Since the symplectic nature of the method is closely related to the periodicity of the Hamiltonian, the symplectic splitting method may have to be adapted to be used in those situations.

The induced currents are in different ways expandable. It is for instance possible to try and find an exact solution to equation (62). If this is not desired, the harmonic truncation could also be taken with a higher order $N > 1$. This will in turn lead to a more complicated fraction in front of the residual currents in equations (14) and (15).

7.4 Future Research

For future research, many new approaches can be taken. The before mentioned change of shape of the bottom-topography with $k \neq l$ or with more Fourier modes might lead to a more complicated residual flow, which may in turn bring about more complicated patterns in the TPS.

Another interesting feature might be the addition of 3D effects in the equations of motion. This would allow for particles to move up and down, this might contribute to the amount of chaos or mixing. In this regard, also effects of wind can be taken into account, leading to relative higher current velocities at the surface of the water compared to the deeper parts of the water.

It might also be interesting to take into account the effect of non-passive particles. In this study the particles did not show any tendency to mix other than those behaviours induced by the tidal and tidal-induced currents. For instance diffusion may be modelled in the equations as noise. This can have consequences for the mixing in the TPS, because particles might 'jump' onto another quasi-periodic orbit, but this can also be viewed mathematically as a dynamical system with (as in configuration 'simple-b') or without chaos (the other configurations) and how this effects the amount of mixing and the value of the largest Lyapunov exponent.

8 Conclusions

The two objectives that we focused on in this study were to investigate what happens when we do take several additional terms in the equations of motion into account, and if it is possible to use a numerical method that preserves the symplectic structure of a Hamiltonian system. To investigate the influence of these additional terms, first a default configuration was numerically solved, to which the configurations with these additional terms could be compared. Using the theory on symplectic splitting methods, we were able to construct a numerical method that preserves the area in phase space for a non-divergent configuration.

The symplectic splitting method, presented in this study, was able to reproduce the qualitative results from Beerens, Ridderinkhof, and Zimmerman 1994. However, the tidal Poincaré section (TPS) produced in this study revealed chaotic particle trajectories for a setting which did not show these chaotic particle trajectories in previous studies. Using harmonic truncation with order 1, an analytic expressions for the relative strength of the residual current was written down. This showed that the previously used value for the relative strength of residual currents was too high. For a more realistic value, which was used in the default experiment, the TPS showed no chaotic trajectories. All trajectories showed quasi-periodic behaviour for this case, with a central elliptic periodic point.

The other investigated configurations, taking into account the Coriolis parameter, a vorticity harmonic term (time-dependent vorticity term), and a divergent term, also showed no signs of mixing in the TPS. This was confirmed by the computation of the largest Lyapunov exponent. For each configuration, except the 'Divergent' configuration the largest Lyapunov exponent was computed for $k * \frac{\pi}{2}$. All computed values of λ converged to zero, thus indicating that for this case the trajectories are not chaotic. For the 'Divergent' configuration, this could not be done, because after a certain amount of tidal periods, the position of the particle was too close to the boundary of the circulation cell to be able to sensibly compute the largest Lyapunov exponent. The number of tidal periods needed show convergence of the value of λ was bigger than the number of tidal periods that it takes to reach the boundary.

For values of k lying very close to the zeroes of the Bessel function $J_0(k)$, which is a special function, the TPS showed that particles travelled a smaller net distance with each Poincaré map. This phenomenon was described by Beerens, Ridderinkhof, and Zimmerman 1994 using the orbit expansion. The orbit expansion suggested that this would lead to the identity map. This identity map was not found in this study. This may be because the symplectic splitting method actually solves a system close to the system it tries to solve, and hence produces a near-identity map.

In this study, the techniques of symplectic splitting methods were successfully applied to a system of differential equations with time-periodic forcing. By applying a time-transformation, the dynamics can be solved as a composition of exactly solved Hamiltonian flows. This numerical method approximates the Poincaré map and preserves the area-preserving property of Hamiltonian flows. It was demonstrated that this is not the case for a standard ode45-solver, which uses a fourth order Runge-Kutta method.

References

- Abdullaev, S. (Apr. 1999). “A new integration method of Hamiltonian systems by symplectic maps”. In: *Journal of Physics A General Physics* 32, pp. 2745–2766. DOI: 10.1088/0305-4470/32/15/004.
- Aref, H. (1983). “Stirring by chaotic advection”. In: *Journal Fluid Mechanics* 143, pp. 1–21.
- Berens, S.P., H. Ridderinkhof, and J.T.F. Zimmerman (1994). “An Analytical Study of Chaotic Stirring in Tidal Areas”. In: *Chaos, Solutions & Fractals* 4.6, pp. 1011–1029.
- Benettin, G. and A. Giorgilli (1994). “On the Hamiltonian interpolation of near-to-the identity symplectic mappings with application to symplectic integration algorithms”. In: *Journal of Statistical Physics* 74, pp. 1117–1143. DOI: <https://doi-org.proxy.library.uu.nl/10.1007/BF02188219>.
- Giardino, Alessio, Giorgio Santinelli, and C. (Kees) Heijer (Jan. 2015). “The State of The Coast - Toestand van de kust Case study: Wadden Islands”. In: DOI: 10.13140/RG.2.1.4640.0481.
- Hairer, Ernst, Christian Lubich, and Gerhard Wanner (2003). “Geometric numerical integration illustrated by the Störmer–Verlet method”. In: *Acta Numerica* 12, pp. 399–450. DOI: 10.1017/S0962492902000144.
- Hirsch, M.W., S. Smale, and R.L. Devaney (2004). *Differential equations, dynamical systems, and an introduction to chaos*. Elsevier(USA).
- Jordan, D and P Smith (2007). *Nonlinear Ordinary Differential Equations: An Introduction for Scientists and Engineers*. Oxford University Press Incorporated, Oxford. ISBN: 9780199208241.
- McLachlan, Robert and G. Quispel (Jan. 2002). “Splitting methods”. In: *Acta Numer.* 11, pp. 341–. DOI: 10.1017/S0962492902000053.
- Ottino, J.M. (1990). “Mixing, Chaotic Advection, and Turbulence”. In: *Fluid Mechanics* 22, pp. 207–253.
- Pasmanter, R. (1988). “Dynamical systems, deterministic chaos and dispersion in shallow tidal flow”. In: *Physical Processes in Estuaries*, pp. 42–53.
- Ridderinkhof, H. and J.T.F. Zimmerman (1992). “Chaotic Stirring in a Tidal System”. In: *Science* 258.5085, pp. 1107–1111.
- Robinson, I.S. (1983). “Chapter 7 Tidally Induced Residual Flows”. In: *Physical Oceanography of Coastal and Shelf Seas*. Ed. by B. Johns. Vol. 35. Elsevier Oceanography Series. Elsevier, pp. 321–356. DOI: [https://doi.org/10.1016/S0422-9894\(08\)70505-1](https://doi.org/10.1016/S0422-9894(08)70505-1). URL: <http://www.sciencedirect.com/science/article/pii/S0422989408705051>.
- Shampine, L. F. and M. W. Reichelt (1997). “The MATLAB ODE Suite”. In: *SIAM Journal on Scientific Computing* 18, pp. 1–22.
- Tabor, M. (1989). *Chaos and Integrebility in Nonlinear Dynamics: An Introduction*. Wiley. ISBN: 9780198520115.
- Vulpiani, A., F. Cecconi, and M. Cencini (2009). *Chaos : From Simple Models to Complex Systems*. Singapore: World Scientific Publishing Company.
- Wang, Daosheng, Qiang Liu, and Xianqing Lv (July 2014). “A Study on Bottom Friction Coefficient in the Bohai, Yellow, and East China Sea”. In: *Mathematical Problems in Engineering* 2014, pp. 1–7. DOI: 10.1155/2014/432529.
- Zervas, C (1999). “Tidal Current Analysis Procedures and Associated Computer Programs”. In: URL: <https://tidesandcurrents.noaa.gov/publications/techrpt21.pdf>.

A Mathematics

A.1 Trigonometric Identities

The trigonometric identities

$$2 \cos \theta \cos \phi = \cos (\theta - \phi) + \cos (\theta + \phi), \quad (60a)$$

$$2 \sin \theta \sin \phi = \cos (\theta - \phi) - \cos (\theta + \phi), \quad (60b)$$

$$2 \sin \theta \cos \phi = \sin (\theta + \phi) + \sin (\theta - \phi), \quad (60c)$$

$$2 \cos \theta \sin \phi = \sin (\theta + \phi) - \sin (\theta - \phi), \quad (60d)$$

with inverse relations

$$\cos (\theta + \phi) = \frac{1}{2} [\cos \theta \cos \phi - \sin \theta \sin \phi], \quad (61a)$$

$$\cos (\theta - \phi) = \frac{1}{2} [\cos \theta \cos \phi + \sin \theta \sin \phi], \quad (61b)$$

$$\sin (\theta + \phi) = \frac{1}{2} [\sin \theta \cos \phi + \cos \theta \sin \phi], \quad (61c)$$

$$\sin (\theta - \phi) = \frac{1}{2} [\sin \theta \cos \phi - \cos \theta \sin \phi], \quad (61d)$$

were used.

A.2 Harmonic Truncation

Harmonic truncation is a technique that is used to approximate the solution of $\hat{\eta}_{k,l}$ to the equation

$$\frac{\partial \hat{\eta}_{k,l}}{\partial t} + ikU\hat{\eta}_{k,l} + r\hat{\eta}_{k,l} = i(fk - rl)U\hat{h}_{k,l}, \quad (62)$$

where $f, k, r, l, \hat{h}_{k,l}$ and U are given, and $i = \sqrt{-1}$ is the imaginary unit. By assumption, the tidal current is a sinusoidal function of time. Since the vorticity is induced by this tidal current, it also has the form of a sinusoidal function, i.e.

$$\hat{\eta}_{k,l} = \eta_0 + \sum_{n=1}^N (\eta_{nc} \cos nt + \eta_{ns} \sin nt), \quad (63)$$

where N is the truncation order of the harmonic truncation, and η_i are the Fourier coefficients. After writing the equation in matrix notation, the solutions for the η_i 's can be found via principles from linear algebra. In the matrix, each row corresponds to a harmonic mode; row one is proportional to 1; row two is proportional to $\cos t$; row three is proportional to $\sin t$; row four is proportional to $\cos 2t$; and so on. Each column corresponds to a prefactor η_i . For truncation order N , the matrix becomes $(2N + 1) \times (2N + 1)$. For the tidal current $U = \cos t$, and truncation order $N = 1$, the equation in matrix notation is

$$\begin{pmatrix} r & \frac{ik}{2} & 0 \\ ik & r & 1 \\ 0 & 1 & r \end{pmatrix} \begin{pmatrix} \eta_0 \\ \eta_{1c} \\ \eta_{1s} \end{pmatrix} = \begin{pmatrix} 0 \\ i(fk - rl)h_{k,l} \cos(t) \\ 0 \end{pmatrix}, \quad (64)$$

with solutions

$$\eta_0 = \frac{k(fk - rl)h_{k,l}}{(k^2 + 2r^2 + 2)}, \quad \eta_{1c} = \frac{2ir(fk - rl)h_{k,l}}{(k^2 + 2r^2 + 2)}, \quad \eta_{1s} = \frac{2i(fk - rl)h_{k,l}}{(k^2 + 2r^2 + 2)}. \quad (65)$$

B Matlab Code

All the numerical integration in this study is done using Matlab. The version that is used is R2020b, August 26 2020.

The structure consists of several code-files. To compute an orbit, the file orbit.m is run. In this file, the input are the different model- and method-parameters, and the output is a tidal Poincaré section for the given parameters. For different initial conditions, the time-evolution is computed. The time-evolution of one time step is computed by calling the function onestep.m. The input for the latter function are the parameters of the system and the current position in phase space (t, p, q) and the size of the timestep Δt (dt in the code). The output are the new coordinates. This function relies on calling different functions for each of the separate Hamiltonians and gradient. These are not all included, but they take the role of calculating the F' and G' as given in equation (32). The explicit function for calculation of the change in position due to the gradient is added. This computation relies on a numerical Newton's method, with accuracy 10^{-12} .

B.1 orbit.m

```
1 clear all
2 close all
3 %parameters of the flows
4 param.k = (2.7)*(pi/2);
5 param.l = param.k;
6 param.f = 1;
7 param.r = 2;
8 param.epsilon = 0.3;
9 param.gammal = 1;
10 param.gamma2 = 1;
11
12 %parameters describing time
13 tides = 400;
14 N = 400;
15 dt = 2*pi/N;
16 Nsteps = tides*N;
17
18 %number of horizontal rows and vertical columns
19 R = 5;
20 C = 7;
21 for j=1:C
22     for i=1:R
23         x = (j/(C+1))*(pi/param.k);
24         y = (i/(R+1))*(pi/param.k);
25
26         X = zeros(1,Nsteps+1);
27         Y = zeros(1,Nsteps+1);
28         X(1) = x;
29         Y(1) = y;
30
31         q = param.k*x + param.l*y;
32         p = param.k*x - param.l*y;
33
34         for n=1:Nsteps,
35
36             tn = (n-1)*dt;
```

```

37         [q,p] = onestep(q,p,dt,tn,param);
38
39         x = (q + p)/(2*param.k);
40         y = (q - p)/(2*param.l);
41
42         X(n+1) = x*(param.k/pi);
43         Y(n+1) = y*(param.l/pi);
44
45     end
46     X(1) = X(1)*(param.k/pi);
47     Y(1) = Y(1)*(param.l/pi);
48     scatter(X(1:N:end),Y(1:N:end), 10, 'filled');
49     hold on;
50 end
51 end
52 hold off
53 %The following improves the look of the plot
54 ax = gca;
55 ax.FontSize = 16;
56 axis([-0.5, 1.5, 0., 1.]);
57 xlabel("x");
58 ylabel("y");

```

B.2 onestep.m

```

1 function [q,p] = onestep(q,p,dt,tn,param)
2     k = param.k;
3     l = param.l;
4     f = param.f;
5     r = param.r;
6     epsilon = param.epsilon;
7     gamma1 = param.gamma1;
8     gamma2 = param.gamma2;
9
10    C1 = 1/(k^2+l^2)/(k^2 +2*r^2 +2);
11    C2 = 1/2/(k^2+l^2);
12
13    alpha1 = -epsilon*k^2*l*C1*(f*k-r*l);
14    beta1 = -epsilon*k^2*l*C1*(f*k+r*l);
15
16    alpha2 = 2*epsilon*k*l*C1*(f*k-r*l);
17    beta2 = 2*epsilon*k*l*C1*(f*k+r*l);
18
19    alpha3 = -epsilon*(k^2+l^2)*k*C2/2;
20    beta3 = -alpha3;
21
22    alpha4 = -epsilon*k*C2/2;
23
24    % H0 step:
25    dtau = sin(tn+dt/2)-sin(tn);
26    q = q + dtau*k;
27    p = p + dtau*k;
28
29    % H1 step:

```

```

30     [q,p] = coscos(q,p,dt/2,alpha1,beta1);
31
32     % H2 step:
33     if gamma1 == 1,
34         dtau = r*(sin(tn+dt/2)-sin(tn)) + cos(tn)-cos(tn+dt/2);
35         [q,p] = sinsin(q,p,dtau,alpha2,beta2);
36     end
37
38     % H3/V3 step (symmetric):
39     if gamma2 == 1,
40         dtau = sin(tn+dt/2)-sin(tn);
41         [q,p] = sinsin(q,p,dtau,alpha3,beta3);
42         dtau = sin(tn+dt)-sin(tn);
43         q = cosgrad2(q,dtau,alpha4);
44         p = cosgrad2(p,dtau,alpha4);
45         dtau = sin(tn+dt)-sin(tn+dt/2);
46         [q,p] = sinsinstar(q,p,dtau,alpha3,beta3);
47     end
48
49     % H2* step:
50     if gamma1 == 1,
51         dtau = r*(sin(tn+dt)-sin(tn+dt/2)) + cos(tn+dt/2)-cos(tn+dt);
52         [q,p] = sinsinstar(q,p,dtau,alpha2,beta2);
53     end
54
55     % H1* step:
56     [q,p] = coscosstar(q,p,dt/2,alpha1,beta1);
57
58     % H0* step:
59     dtau = sin(tn+dt)-sin(tn+dt/2);
60     p = p + dtau*k;
61     q = q + dtau*k;

```

B.3 cosgrad.m

```

1 function q = cosgrad(q,dt,alpha);
2 %
3 % Solve q' = alpha*cos(q) for a step of size dt
4 %
5 maxIter = 100;
6 tol = 1e-12;
7
8 qh = q + dt/2*alpha*cos(q);
9
10 for k=1:maxIter,
11
12     r = qh - q - dt/2*alpha*cos(qh);
13     J = 1;
14     qh = qh - r/J;
15
16     if abs(r)<tol
17         break;
18     end
19 end

```



```

20
21     if k>=maxIter
22         error('Newton failed to converge');
23     end
24
25     q = 2*qh - q;
26
27 end

```

B.4 lyapunov.m

This is the Matlab code that is used to compute the largest Lyapunov exponent of the method for an initial condition.

```

1  clear all
2  close all
3  %parameters of the flows
4  param.k = (2.7)*(pi/2);
5  param.l = param.k;
6  param.f = 0;
7  param.r = 2;
8  param.epsilon = 0.3;
9  param.gamma1 = 0;
10 param.gamma2 = 0;
11 eps = 10^(-8);
12
13 %parameters describing time
14 tides = 50000;
15 N = 200;
16 dt = 2*pi/N;
17 Nsteps = tides*N;
18
19 %initial condition
20 x = (5/6)*(pi/param.k);
21 y = (7/8)*(pi/param.k);
22 v = [1, -1];
23
24 %conversion to parameters for the calculation
25 q = param.k*x + param.l*y;
26 p = param.k*x - param.l*y;
27
28 r = sqrt(v(1)^2 + v(2)^2);
29 v = v/r;
30 r_sum = log(1);
31 xt = x + eps*v(1);
32 yt = y + eps*v(2);
33
34 qt = param.k*xt + param.l*yt;
35 pt = param.k*xt - param.l*yt;
36
37 R = zeros(1, Nsteps+1);
38 R(1) = log(1);
39 for n =1:Nsteps
40     tn = (n-1)*dt;
41     %calculation of new points

```

```

42     [q,p] = onestep(q,p,dt,tn,param);
43     x = (q + p)/(2*param.k);
44     y = (q - p)/(2*param.l);
45     [qt, pt] = onestep(qt,pt,dt,tn,param);
46     xt = (qt + pt)/(2*param.k);
47     yt = (qt - pt)/(2*param.l);
48     %computation of r_n and v_n
49     v = [xt-x, yt-y]*(1/eps);
50     r = (sqrt(v(1)^2 + v(2)^2));
51     v = v/r;
52     r_sum = r_sum + log(r);
53     R(n+1) = r_sum/n/dt;
54     %resetting the perturbation
55     xt = x + eps*v(1);
56     yt = y + eps*v(2);
57     qt = param.k*xt + param.l*yt;
58     pt = param.k*xt - param.l*yt;
59 end
60 plot(R);
61 Lyapun = r_sum/Nsteps/dt
62 % The following improves the quality of the diagram
63 ax = gca;
64 xlabel("Nsteps (Iterations)");
65 ylabel("Lyapunov exponent");
66 set(gca, 'xscale', 'log');
67 set(gca, 'yscale', 'log');

```

C Identification with earlier study

In the study (Beerens, Ridderinkhof, and Zimmerman 1994) a system very similar to the model of section 2 is used. To refer to this study and the system therein, here, the subscript b is used to explicitly refer to the system from (Beerens, Ridderinkhof, and Zimmerman 1994).

$$\begin{aligned}\frac{\partial x_b}{\partial t_b} &= \pi \lambda_b \cos 2\pi t_b + \pi \nu_b \lambda_b \sin \pi x_b \cos \pi y_b, \\ \frac{\partial y_b}{\partial t_b} &= -\pi \nu_b \lambda_b \cos \pi x_b \sin \pi y_b.\end{aligned}\tag{66}$$

This can be transformed into our system via the transformation

$$(x, y) = \alpha(x_b, y_b), \quad k = \frac{\pi}{\alpha}, \quad t = 2\pi t_b.\tag{67}$$

The transformation of the derivative of x_b thus becomes

$$\frac{dx_b}{dt_b} = \frac{dt}{dt_b} \frac{dx_b}{dt} = \frac{dt}{dt_b} \frac{d}{dt} \left(\frac{x}{\alpha} \right) = \frac{2\pi}{\alpha} \frac{dx}{dt}.\tag{68}$$

The derivative of y_b transforms in a similar way. Our equation for \dot{x}_b , with transformed coordinates becomes

$$\dot{x}_b = \frac{2\pi}{\alpha} \cos 2\pi t_b + \frac{[h]}{H} \frac{r \left(\frac{\pi}{\alpha} \right)^2}{\left(\frac{\pi}{\alpha} \right)^2 + 2r^2 + 2} \sin(\pi x_b) \cos(\pi y_b).\tag{69}$$

We can now identify, by comparing to (66),

$$\frac{2\pi}{\alpha} = \pi \lambda_b, \quad \text{s.t. } \alpha = \frac{2}{\lambda_b}, \quad \text{and } k = \frac{\pi \lambda_b}{2},\tag{70}$$

which leads to

$$\pi \lambda_b \nu_b = \frac{r \left(\frac{\pi}{\alpha} \right)^2}{\left(\frac{\pi}{\alpha} \right)^2 + 2r^2 + 2} = \frac{r(\pi \lambda)^2}{4 \left(\left(\frac{\pi \lambda}{2} \right)^2 + 2r^2 + 2 \right)}.\tag{71}$$

A function for ν_b , to identify the two systems can now be written down:

$$\nu_b = \frac{[h]}{H} \frac{rk}{2(k^2 + 2r^2 + 2)}.\tag{72}$$

This function has a maximum for $k = \sqrt{2(r^2 + 1)}$, then taking the limit of $r \rightarrow \infty$, which leads to the value

$$\nu_{\max} = \frac{[h]}{H} \frac{\sqrt{2}}{8}.\tag{73}$$

Since $[h] \ll H$, this value is lower than $\frac{\sqrt{2}}{8} \approx 0.17$. The value as used by (Beerens, Ridderinkhof, and Zimmerman 1994) ($\nu = 0.3$) is thus not realistic. These relations are derived from a solution of the harmonic truncation (section A.2 with $N = 1$. Taking $N = 2$, still leads to a similar discrepancy between the value for ν_{\max} and the value $\nu_b = 0.3$.